

RESEARCH ARTICLE

10.1002/2015JC010796

Internal tides and tidal cycles of vertical mixing in western Long Island Sound

Grant McCardell¹, James O'Donnell¹, Alejandro J. Souza², and Matthew R. Palmer²¹Department of Marine Sciences, University of Connecticut, Groton, Connecticut, USA, ²National Oceanography Centre, Liverpool, UK

Key Points:

- Internal waves and tides in Long Island Sound are observed by moored sensors.
- The occurrence of internal waves relates to near-bottom scalar tendencies.

Correspondence to:

G. McCardell,
grant.mccardell@uconn.edu

Citation:

McCardell, G., J. O'Donnell, A. J. Souza, and M. R. Palmer (2016), Internal tides and tidal cycles of vertical mixing in western Long Island Sound, *J. Geophys. Res. Oceans*, 121, 1063–1084, doi:10.1002/2015JC010796.

Received 19 FEB 2015

Accepted 6 JAN 2016

Accepted article online 12 JAN 2016

Published online 1 FEB 2016

Abstract In estuaries, tidal period variations in the rate of vertical mixing have been observed to result from various causes: in Liverpool Bay and the York River, they have been attributed to tidal straining of the along-channel density gradient modulating stratification; in the Hudson River they arise from tidal modulation of the height of the tidal current bottom boundary layer (BBL). Along continental shelves, tidal period fluctuations in mixing have been observed to result from the dissipation of internal waves (IW). Western Long Island Sound (WLIS) moored instrument records indicate that large near-bottom increases in dissolved oxygen (DO) and heat and a decrease in salt occur during the middle of the flood tide: an analysis of water mass signatures indicates that the transport involved is vertical and not horizontal. Temperature data from a vertical thermistor array deployed in the WLIS for 16 days in August 2009 clearly show a tidal cycle of IW activity creating a mean thermocline depression at mid-flood of approximately 25% of the water depth with individual IW thermocline depressions of as much as 50% of the water depth. Contemporaneous ADCP measurements show increases in shear due to IWs during the flood. Near-bottom internal wave activity is maximal at and after midflood and is correlated with near-bottom temperature and DO tendencies at both tidal and subtidal scales. We conclude that internal tides are an important vertical mixing mechanism in the WLIS through both increased shear from IWs and displacement of the pycnocline into the region of high shear in the BBL.

1. Background

1.1. Long Island Sound

Long Island Sound (LIS) is a semienclosed estuary on the east coast of the United States. Its main communication with the Atlantic is through the Race at its eastern end with estimates of this exchange ranging between 4000 and 23,000 m³ s⁻¹ [O'Donnell *et al.*, 2014]. LIS has a secondary connection to the Atlantic through its western end via the East River and New York Harbor, but the subtidal exchange is estimated at only 310 m³ s⁻¹ [Blumberg and Pritchard, 1997]. LIS tides are predominately M₂ and are close to being in resonance in the basin. Tidal height amplitudes increase from 0.25 m at the eastern end to 1.1 m at the western end. Tidal currents vary from as much as 2 m s⁻¹ in portions of the Race to below 20 cm s⁻¹ at the western end of the Sound [Bennett *et al.*, 2010].

The width of LIS increases from about 12 km at the Race to a maximum of 20 km in the central Sound and then decreases to less than a kilometer at the Throg's Neck at the western end. The bathymetry is quite variable in the energetic Race where depths range up to 100 m, but most of LIS is considerably flatter with a mean depth of approximately 20 m. The western LIS (WLIS) is moderately stratified during the summertime with surface to bottom density differences on the order of 2 kg m⁻³ caused fairly equally by temperature and salinity gradients [Gay *et al.*, 2004].

The bottom waters of the WLIS experience seasonal hypoxia in the summertime. This results from a small difference between the water column respiration demand and the rate of transport [O'Donnell, *et al.*, 2008 and McCardell and O'Donnell, 2014]. Because of this near balance, changes in the transport supply can change the sign of the net rate of change (or tendency). Variation in the rate of decline of dissolved oxygen (DO) in the July and August time due to variability in physical transport is evidenced by the correlation of DO tendencies with synoptic scale weather effects described by O'Donnell *et al.* [2008] and by the correlation between effective vertical eddy diffusivities and DO tendencies observed by McCardell and

O'Donnell [2009]. It also seems clear from McCardell and O'Donnell [2014] that the bulk of the physical resupply is due to vertical processes. The relative importance of the mechanisms that control these vertical processes and their variability has, however, remained unclear.

1.2. Mixing in Estuaries

It is often taken that mixing due to shear instabilities results when the gradient Richardson number, $Ri \equiv N^2/S^2$, where N is the Brunt-Väisälä buoyancy frequency and $S^2 = (\partial \mathbf{u} / \partial z)^2$ is the shear squared, falls below a threshold value [MacKinnon and Gregg, 2005]. The vertical turbulent flux of a scalar concentration, C , can be modeled as $-K_V \partial C / \partial z$ where K_V is an eddy coefficient, and there have been numerous schemes that relate Ri and K_V . These range from the simple algebraic formulation of Munk and Anderson [1948] to the turbulence closure schemes of Mellor and Yamada [1982] and others [Umlauf and Burchard, 2005]. All predict a monotonic decrease in K_V with increasing Ri .

Modulation of Ri will occur when either the shear or stratification varies. Ri can vary greatly throughout a tidal cycle. Whitney et al. [2012] compare a number of estuaries in order to determine whether variability in stratification or variability in shear predominates tidal variability in Ri . They find that modulation of Ri is generally caused by changes in stratification, though in some regions, variability in shear dominates. In this study, we examine the relative importance of stratification and shear to the modulation of diapycnal mixing in the WLIS. We also investigate the possible importance of internal waves and internal tides to mixing in the WLIS.

Examples of the modulation of rates of vertical mixing through tidal variation in stratification are sometimes seen when there are longitudinal density gradients in addition to vertical (i.e., sloped pycnoclines) since differential advection of the along-channel gradient will result in modulation of the vertical density gradient [Simpson et al., 1990]. Since most estuaries exhibit an along-channel density gradient due to greater salinities near the mouth, this mechanism can result in decreased stratification and therefore increased mixing toward the end of the flood and increased stratification, and therefore less mixing, toward the end of the ebb. This type of tidal straining has been extensively studied in Liverpool Bay where mixing is seen to occur predominantly toward the end of the flood [Rippeth et al. 2001], and in the York River, VA, where spring-neap variability in the straining results in a fortnightly variability in mixing [Sharples et al., 1994].

The modulation of mixing through variability in shear has been observed in the Hudson River. Through the use of dye tracers, Chant et al. [2007] were able to show that BBL growth during the flood tide in the Hudson River was sufficient for the bottom shear layer to impinge upon the pycnocline, resulting in entrainment of pycnocline water by the bottom boundary shear layer. They observed significant spring-neap variability in this mixing with the bottom boundary layer being considerably thicker resulting in intensified mixing during spring tides.

In stratified flows, internal waves can be responsible for significant amounts of vertical mixing due both to wave breaking and Kelvin-Helmholtz instabilities [Burchard, 2002]. Internal waves have been associated with the propagation and dissipation of tidal energy on the continental shelves [Colosi et al., 2001; Garrett and Munk, 1979; Jackson, 2004; Munk and Wunsch, 1998]. Internal wave trains, generated by across-isobath tidal flows over the shelf break, are credited with creating regions of enhanced mixing as the soliton trains of the internal tide propagate across the shelf. Increased mixing due to increased shear associated with these internal waves or with internal wave shoaling and breaking has been extensively observed on the continental shelves [Hosegood and van Haren, 2004; Müller and Briscoe, 2000; Lien and Gregg, 2001; Moum et al., 2003]. Although it seems plausible that internal waves generated by tidal flows could likewise be responsible for regions of enhanced mixing in estuaries, direct observations of internal waves have been less frequently reported on in estuaries than on the shelves. Henyey [1999] described solibore and internal wave observations in Knight Inlet, British Columbia. Bourgault and Kelley [2003] reported on observations of internal waves generated during flood tides in the St. Lawrence estuary and inferred enhanced mixing from model results based on their observations. More recently, Helda et al. [2013] observed tidally generated internal waves in the Ems estuary creating enhanced mixing during the ebb due to increased shear.

2. Observations

In order to investigate vertical transport mechanisms in the WLIS, in 2009, we deployed a bottom mounted ADCP operating in coherent frequency mode (RDI mode 12) and recording at 1 Hz frequency for 60 s every 5 min (ADCP1), a second ADCP also operating in coherent mode and recording at 1 Hz continuously

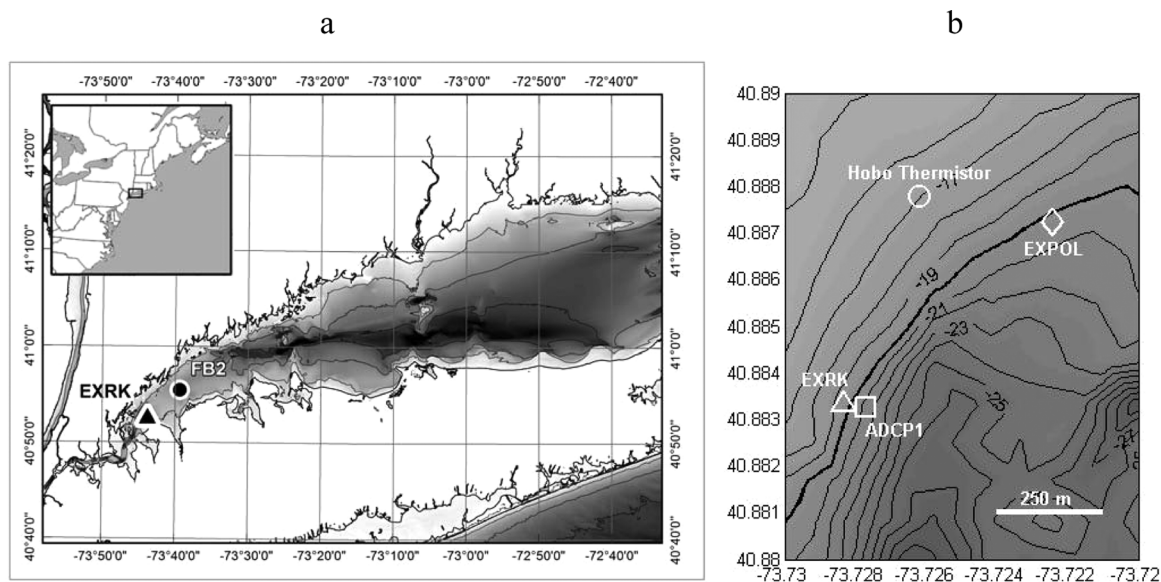


Figure 1. Location of the deployment. The triangle in Figure 1a shows the location of the EXRK buoy (NOAA 44022) in the WLIS with 10 m bathymetry contours. (b) Instrument locations and the local bathymetry with 1 m contours. The -20 m contour is shown in Figure 1b by the heavier black line. The inset in Figure 1a shows the location of the WLIS on the eastern U.S. coast.

(EXPOL), and a thermistor array with 17 Hobo temperature loggers at 1 m intervals recording at a frequency of 1 min^{-1} (Hobo thermistor string). The two ADCPs and the thermistor chain were deployed within 700 m of each other with ADCP1 at $40^{\circ}52.995'N$ $73^{\circ}43.663'W$ in 21.15 m mean water depth, EXPOL at $40^{\circ}53.235'N$ $73^{\circ}43.346'W$ in 20.2 m mean water depth, and the thermistor chain at $40^{\circ}53.268'N$ $73^{\circ}43.574'W$ in 18.5 m mean water depth. ADCP1, EXPOL, and the thermistor string were deployed for 16 days from 28 July 2009 to 14 August 2009. Due to battery limitations, the EXPOL ADCP only recorded from 30 July through 7 August and from 12–14 August. The NERACOOS EXRK buoy at $40^{\circ}53.00'N$ $73^{\circ}43.70'W$ (NOAA designation 44022) in 22.6 m mean water depth was operational during the entire deployment period and it recorded temperature, salinity, and DO at near-surface (-0.25 m; YSI 6600V2), mid depth (-6.0 m; Seabird SBE19+V2), and near-bottom (-16.2 m; Seabird SBE19+V2) depths at a 15 min sampling interval. Figure 1 shows the location of the two ADCPs, the Hobo thermistor string and the EXRK buoy.

ADCP1 provides a record of the mean tidal current structure near EXRK for the deployment period while the EXPOL ADCP provides an additional record of this as well as detailed structure of higher-frequency events. The EXRK buoy provides the tidal and subtidal evolution of salinity, temperature, and DO while the Hobo thermistor string provides both increased vertical and temporal resolution of temperature and a record of fluctuations caused by displacements of the thermocline by internal waves and tides. Prior to the deployment, the 17 Hobo thermistors were tested in the laboratory using a Seabird SBE-19 CTD as a cross reference in order to determine response times and biases. No significant biases were found, and an e -folding response time of 150 ± 30 s to abrupt changes in temperature was consistent among the 17 Hobo instruments.

Figure 1 shows that ADCP1, EXRK, and the thermistor chain were not spatially coincident, and the water depths at their locations were slightly different. Before performing any calculations involving multiple data sets, the instrument depths were transformed into sigma coordinates (where $\sigma = -1$ is the bottom and $\sigma = 0$ is the free surface) as $\sigma = (z - \eta) / (H + \eta)$ with z being the earth coordinate, η the time-dependent free surface elevation determined from the ADCP1 pressure record, and H the mean water depth.

Weather conditions during the deployment were fair. Figure 2 shows air temperatures (a), winds (b), near-bottom DO levels (c), and near-bottom temperatures (d) at the EXRK buoy during the period of the deployment. Air temperatures ranged between 20°C and 30°C . Winds were generally from the SSW and under 5 m s^{-1} , although toward the end of the 16 day deployment, these were from the NE. O'Donnell *et al.* [2008] hypothesize that winds from this direction act to slow the gravitationally driven residual estuarine circulation and result in increased mixing due to the inhibition of the rate of restratification. Note that both near-

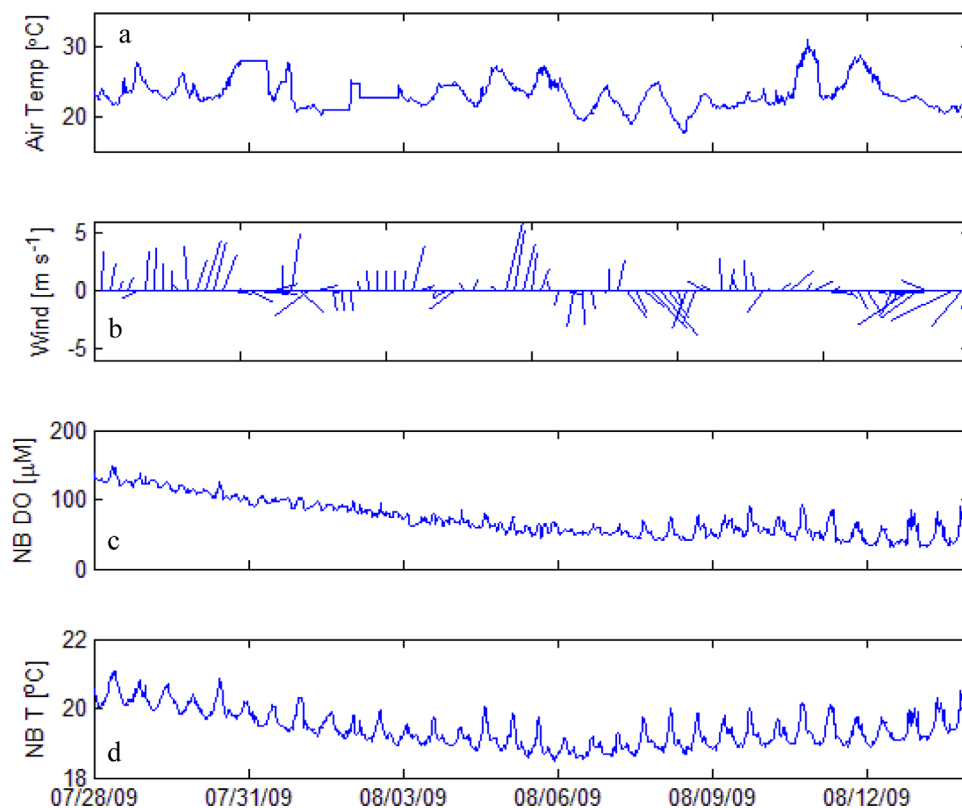


Figure 2. (a) Air temperatures ($^{\circ}\text{C}$), (b) 3 h mean wind vectors (m s^{-1}), (c) near-bottom DO (μM), and (d) near-bottom temperatures ($^{\circ}\text{C}$) at the EXRK buoy during the 16 day deployment. The direction of the vectors in Figure 2b indicate the direction the wind blew to.

bottom temperature and DO show mean declines during the first half of the deployment. The increase in noise toward the end of the DO and temperature records is discussed in section 4.

Figure 3 shows the mean along and across-channel velocities by depth and phase (relative to near-bottom maximum ebb at ADCP1) obtained from the ADCP1 and EXPOL data records. The phase-averaging methodology used is described in Appendix A. Fifty-six degree east of north was used as the along-Sound axis: this corresponds with the near-bottom major axis at EXRK reported by Bennett *et al.* [2010]. The top plots of Figure 3 show the velocity structure at ADCP1 while the bottom plots show this at EXPOL. Because LIS is near resonance, tidal currents and tidal heights in this area are near quadrature and the times of low water (LW) and high water (HW) both occur near slack water. Note the large amplitude of the M_6 frequency (sixth diurnal) as commented upon by Bennett *et al.* [2010] modulates the near-bottom flood-tide currents causing these to show two peaks in maximum velocities during the flood.

3. Results and Analysis

3.1. Tidal Cycle of Ri

Because a high correlation between temperature and salinity is observed in the EXRK buoy records ($r = 0.92$), the temperature records of the Hobo thermistor string are able to be used to estimate proxy salinities. The thermistor temperatures and the proxy salinities were used with the UNESCO (1983) equation of state [Morgan, 1998] to calculate proxy densities. Figure 4a shows the tidal evolution of the phase-averaged \log_{10} buoyancy frequency squared, $N^2 = -g/\rho_0 \cdot \partial\rho/\partial z$, at the thermistor string calculated from the proxy densities. The depression and weakening of the pycnocline seen after the maximum flood in Figure 4a is discussed in a later section.

Prior to calculating the shear-squared, $S^2 = (\partial u/\partial z)^2 + (\partial v/\partial z)^2$, the velocity records of ADCP1 and EXPOL were filtered using a low-pass raised cosine filter with a $8 \cdot 10^{-4}$ Hz cutoff (20 min period). This enables the two velocity records (with different sampling frequencies) to be compared with similar noise levels. Figures 4b and 4c show

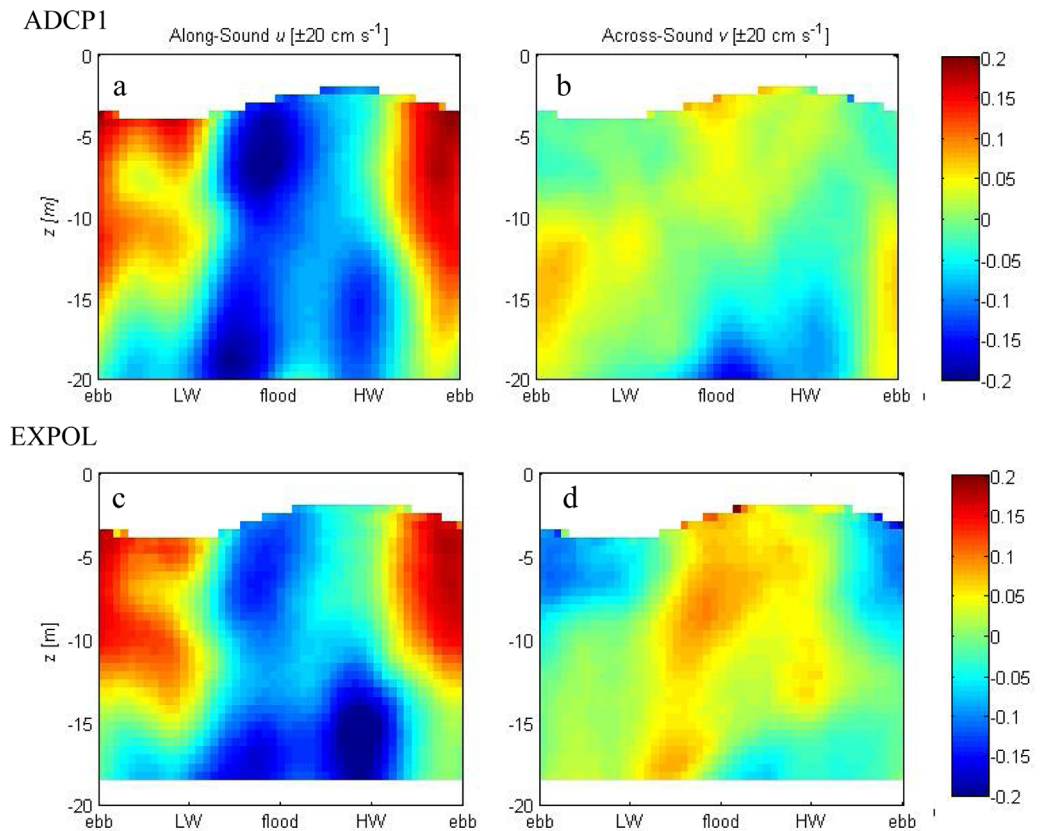


Figure 3. (left-hand: a, c) Along-Sound and (right-hand: b, d) across-Sound tidal velocity structures determined through the phase-averaging methodology described in Appendix A. The Figures 3a and 3b show the structure at ADCP1 for the 16 days of the deployment; the Figures 3c and 3d show the structure at EXPOL for the 10 days of its operation. All four plots use a color range of $\pm 0.2 \text{ m s}^{-1}$ and 56° east of north was used as the along-Sound axis with positive u being an ebb flow in this direction. The horizontal labels “ebb” and “flood” represent maximum near-bottom ebb and flood at the M_2 frequency. “LW” and “HW” represent the low and high water slacks at the M_2 frequency.

the evolution of the mean \log_{10} shear squared at ADCP1 and EXPOL by tidal phase and sigma level. For both N^2 and S^2 , 10^{-6} s^{-2} was used as the noise floor in order to avoid the singularity at zero and imaginary results. Both ADCP results show a period of increased shear near the surface around the time of slack water at the end of the ebb and beginning of the flood. Both ADCP1 and EXPOL show regions of increased shear near the pycnocline ($\sigma \cong -0.25$) during low water at the time of late ebb/early flood. EXPOL also shows a period of increased shear in the lower layer ($\sigma \cong -0.7$) during the start of the ebb that is not seen at ADCP1.

The estimates of the shear-squared, S^2 , and the buoyancy frequency squared, N^2 , shown in Figures 4a–4c can be combined to estimate the tidal evolution of the gradient Richardson number, $Ri = N^2/S^2$. Figure 4d shows estimates of Ri using ADCP1 and the thermistor string and 4e shows the estimates using EXPOL and the thermistor string. Although there are differences between the two sets of estimates, both show regions of minimum Ri during midflood at sigma levels between -0.3 and -0.2 and during late ebb at sigma levels between -0.8 and -0.7 . EXPOL also shows a secondary Ri minimum occurring at this depth during late flood. This corresponds to the region of increased shear in the lower layer during the start of the ebb that is seen in Figure 4c. At pycnocline depths ($-0.5 \leq \sigma \leq -0.22$), Ri maxima occur during late flood and early ebb. Figure 4 indicate that this Ri maxima is largely due to reduced shear, not increased stratification.

Figure 5 shows the depth averages by tidal phase and the tidal averages by depth of \log_{10} of the buoyancy frequencies squared (Figure 4a, blue), shear-squared (Figures 4b and 4c, red), and gradient Richardson numbers (Figures 4d and 4e, black). The results obtained from the ADCP1 and EXPOL records are shown by the light-dashed and light solid lines, respectively, while the results obtained by averaging the ADCP1 and EXPOL results are shown by the heavy lines. Figures 5a and 5b show the depth average of sigma levels where results were present for all tidal phases ($-0.85 \leq \sigma \leq -0.22$) while Figures 5e and 5f [AQ3] show the depth average of sigma levels in the region of the pycnocline ($-0.5 \leq \sigma \leq -0.22$).

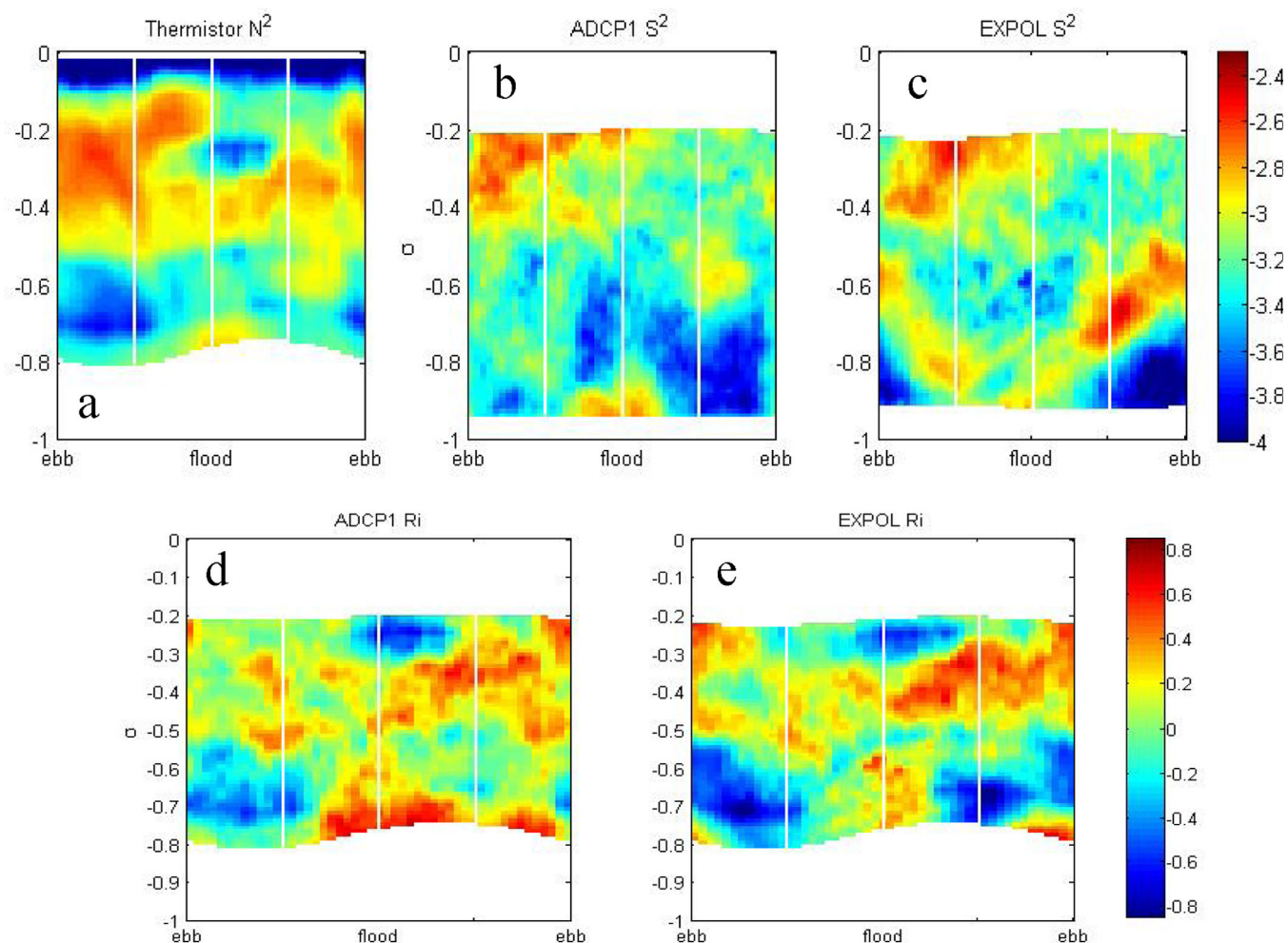


Figure 4. (a) Phase averages of \log_{10} of the buoyancy frequency squared, N^2 ($s^{-2} \cdot 10^{-3}$), at the thermistor chain; the shear-squared, S^2 ($s^{-2} \cdot 10^{-3}$), at (b) ADCP1 and (c) EXPOL; and the gradient Richardson numbers, $\log_{10}(Ri)$ Ri , calculated using the shear-squared from (d) ADCP1 and (e) EXPOL by sigma depth and M_2 phase. The horizontal labels “ebb” and “flood” represent maximum near-bottom ebb and flood at ADCP1 at the M_2 frequency.

Figure 5c shows that the depth of maximum stratification, as indicated by the maximum N^2 shown in blue, and indicative of the mean pycnocline depth, occurs at a sigma level of approximately -0.35 . Figure 5e shows that in the region of the pycnocline, the minimum stratification (blue) occurs during mid flood while the maximum shear (red) occurs during the late ebb. Minimum Ri values within the pycnocline occur during the midflood at the time of minimum stratification.

3.2. BBL Heights

Although the bottom boundary layer velocities are largely unresolved, *Chant et al.* [2007] showed that ADCP records allow the estimation of maximum BBL heights as the level of the maximum above-bottom current where the velocity shear is a local minimum. This method was applied to each tidal cycle of the ADCP1 record by visual inspection of the unfiltered record. Maximum BBL heights for all tidal cycles occurred during the flood, but for the 31 tides of the 16 day deployment, the BBL rarely exceeded 25% of the water column depth at the ADCP1 location.

3.3. Internal Waves and Tides

Visual inspection of the thermistor chain temperature records reveals many regions which are indicative of internal wave activity at periods of 5–10 min. Figure 6a shows water temperatures from the entire thermistor record while 8b shows a 3 day detail. The vertical white lines in Figure 6a show the times of maximum

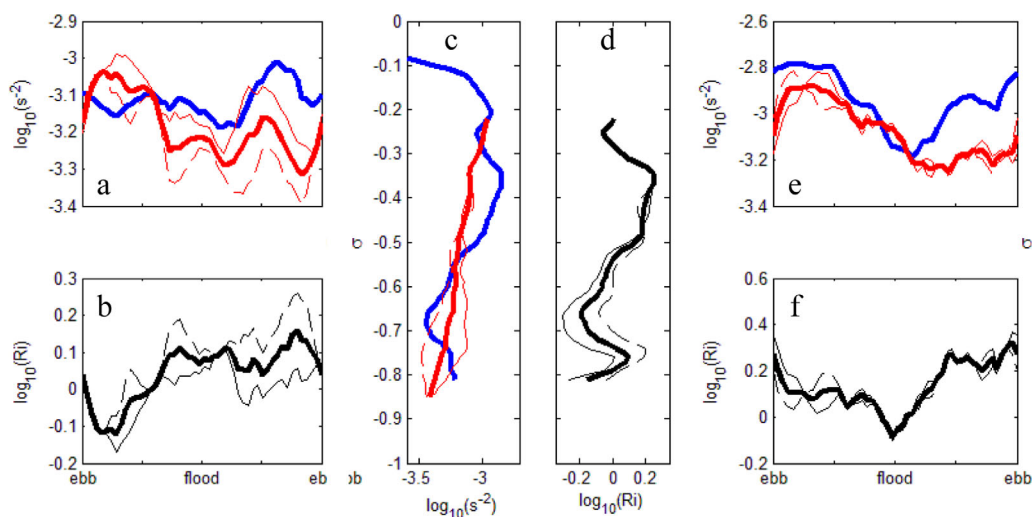


Figure 5. Depth averages of the accessible water column (a, b; $-0.85 \leq \sigma \leq -0.22$), tidal-averages (c, d), and depth-averages within the region of the pycnocline (e, f; $-0.50 \leq \sigma \leq -0.22$) of \log_{10} of buoyancy frequencies squared (blue), shear-squared (red), and gradient Richardson numbers (black) shown in Figures 4 and 5. For both the shear-squared and the gradient Richardson numbers, the thin-dashed and thin solid lines show the results from ADCP1 and EXPOL, respectively, while the heavy solid lines show the means of these two results. The depth averages (a, b, e, f) are shown by tidal phase relative to maximum near-bottom ebb at ADCP1. The tidal-averages (c, d) are shown by sigma depth.

near-bottom flood as determined from the ADCP1 record. Figure 6b highlights the tidal “sawtooth” pattern that is a characteristic of nonlinear internal tides in shallow water [Henyey, 1999].

Figure 7 shows the phase averages of the internal wave activity at the lowest thermistor depth, $z = -16.5$ m, as the high-passed ($8 \cdot 10^{-4}$ Hz) variance (spectral energy) of the temperatures. The 150 s response time of the Hobo thermistors acts as a real-time low-pass filter with a $7 \cdot 10^{-7}$ Hz (150 s period) cutoff, so the variances shown in Figure 7 should be considered as being band-passed at internal wave frequencies of $8 \cdot 10^{-4} - 7 \cdot 10^{-3}$ Hz (periods of 2.5–20 min). Although Figure 7 indicates that most of the near-bottom internal wave activity occurs during the mid to late flood, some activity also occurs during the first half of the ebb.

Figure 8 shows a 2 h portion of the thermistor record, detailing the passage of a soliton train that occurred during the early portion of the ebb tide on 28 July. It is interesting to observe that the second soliton in the train shown in Figure 8 has the maximum amplitude whereas theory predicts that the leading soliton in this type of “packet” will have the maximum amplitude [Jackson, 2004]. The pattern observed here is virtually identical to that observed by Henyey [1999] in Knight Inlet, BC where he also noted that the second soliton amplitude exceeded the first. As exemplified by Figure 8, the internal waves observed in the thermistor record are internal waves of depression, meaning they represent coherent depressions of isotherms from the near-surface into lower waters.

The thermistor record was also used to estimate maximum internal wave depression depths by tidal cycle. This was determined for each tidal cycle by finding the lowest depth to which an isotherm at -5 m descended. The difference between the -5 m “starting point” and this depth is representative of the maximum depression of an internal wave during that tidal period. Figure 9a shows these results for each of the thirty M_2 periods that were covered by the thermistor record. This methodology also includes any mean isotherm depression or internal tide that occurs during the tidal cycle. The net change in near-bottom temperatures and DO that occurred during each of the tidal cycles are shown in Figures 9b and 9c. These both show weak positive correlations ($r = 0.54$, $p = 0.001$; $r = 0.17$, $p = 0.18$) to the magnitudes of the depressions shown in Figure 11a.

The 1 Hz sampling rate of the EXPOL ADCP allowed resolution of the velocity structures of internal waves for the periods it was active. The EXPOL velocity records were band-pass filtered to exclude energy at periods above 20 min and below two minutes using a raised cosine band-pass filter with half power points of $8 \cdot 10^{-4}$ and $8 \cdot 10^{-3}$ Hz, respectively (periods of 2–20 min). After this filtering, internal wave train events were

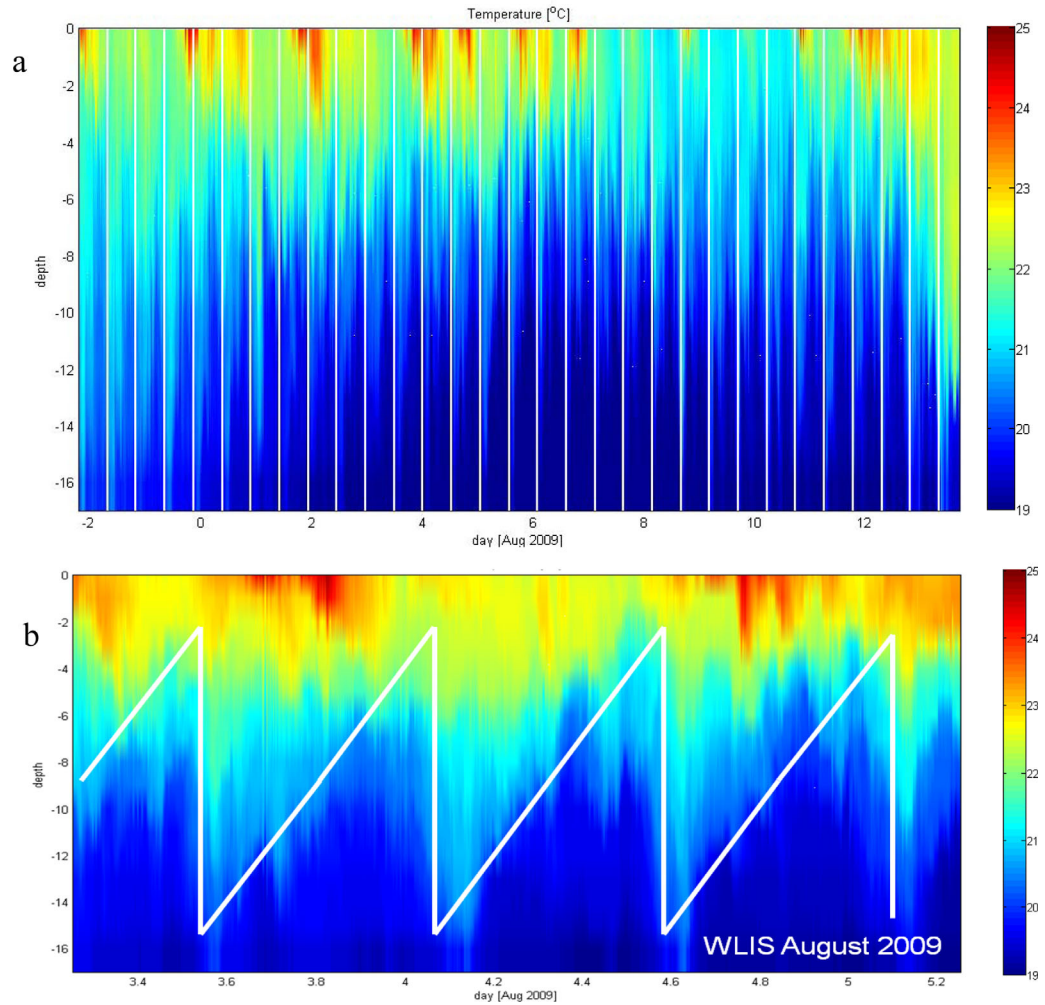


Figure 6. (a) The entire 16 day WLIS Hobo thermistor record ($^{\circ}\text{C}$) by depth (ordinate axis, m) and time (abscissa axis, days). The time of maximum near-bottom flood at the M_2 frequency as determined by ADCP1 is shown by the vertical white lines. Figure 6b shows a 2 day detail highlighting the “sawtooth” pattern that is characteristic of a nonlinear internal tide in shallow water.

evident in both the horizontal and vertical EXPOL velocity records. When the internal wave events observed in the EXPOL ADCP record are compared with coincident records from the Hobo thermistor chain, some events correspond, while others do not. Since the instruments are not collocated, the two records should be lagged by $x/(c \cos \theta)$ where c is a propagation velocity, $x \cong 325$ m is the distance between the Hobo thermistor array and EXPOL (see Figure 1b), and where θ is the angle between the propagation direction and the direction of a line between the thermistor chain and the EXPOL ADCP. A propagation velocity on

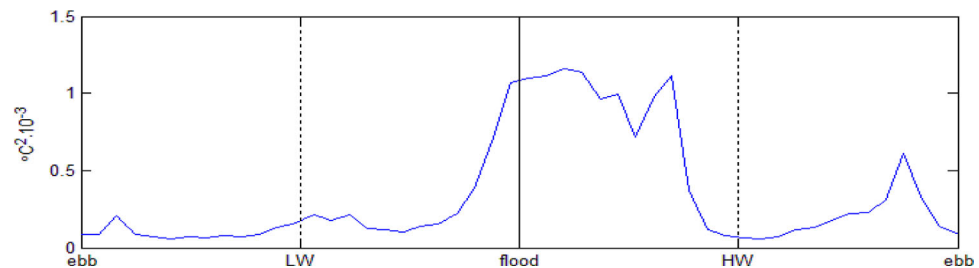


Figure 7. Mean near-bottom internal wave activity as the tidal phase averages of the high-passed ($f_0 = 8 \cdot 10^{-3}$ Hz) variance ($^{\circ}\text{C}^2 10^{-3}$) at the bottom sensor on the thermistor chain. The horizontal labels “ebb” and “flood” represent maximum near-bottom ebb and flood at the M_2 frequency at ADCP1.

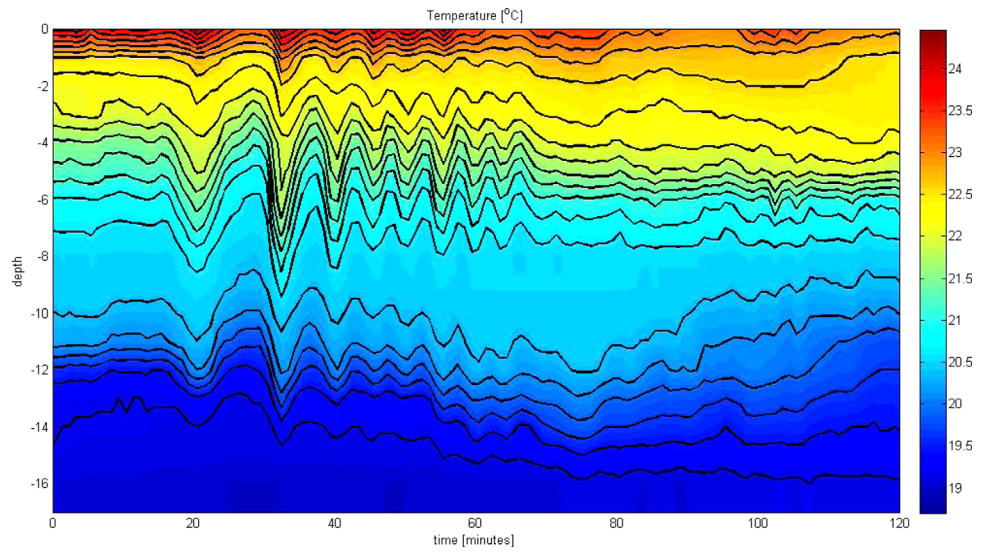


Figure 8. 120 min detail of the thermistor temperature record showing the passage of an internal soliton train during the start of the ebb on 28 July 2009.

the order of 25 cm s^{-1} implies anywhere from a 20 min lead to a 20 min lag between the two sets of observations, depending on the propagation direction. Figure 12 shows an internal wave event that occurred on a flood tide. Thorpe [2005] shows that the number of reversals in horizontal velocities in an internal wave is determined by the internal wave’s mode of oscillation. As indicated by regions where red and blue alternate by depth, the horizontal velocities in Figure 10 show multiple reversals by depth, indicating high mode events. This is particularly true for events occurring during the flood. The events observed during the flood also appear to show a clockwise rotation of the horizontal velocity vector with increasing z (toward the surface).

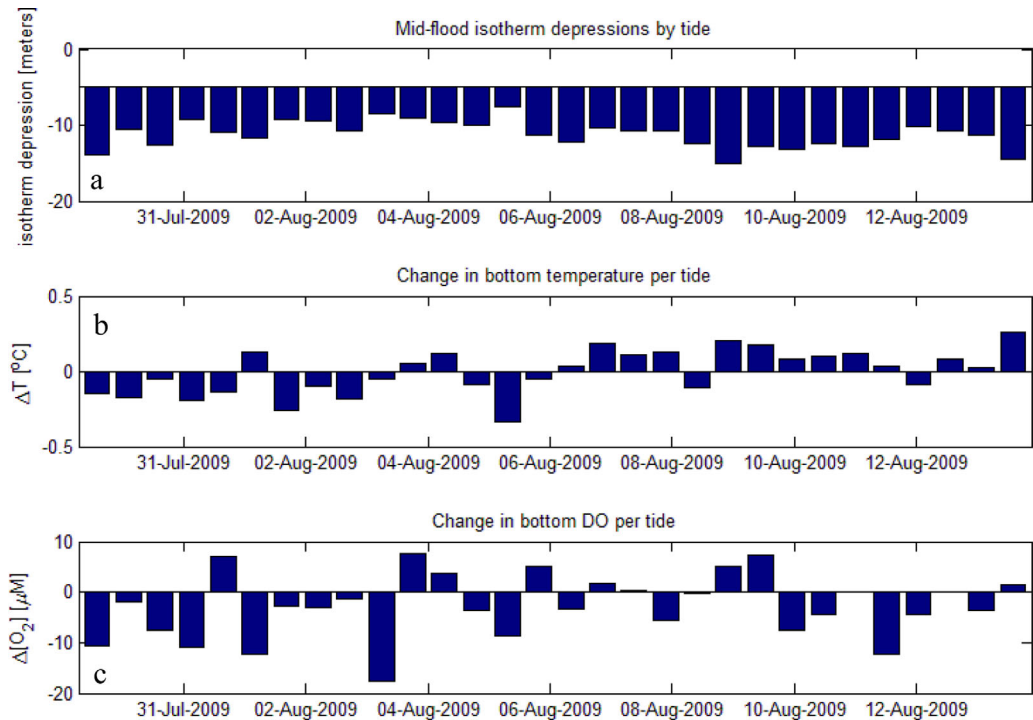


Figure 9. (a) Depths of maximum depression of the -5 m isotherms (m), (b) net change in near-bottom temperature ($^{\circ}\text{C}$), and (c) net change in near-bottom DO (μM) per M_2 tidal cycle (maximum near-bottom ebb to maximum near-bottom ebb at ADCP1).

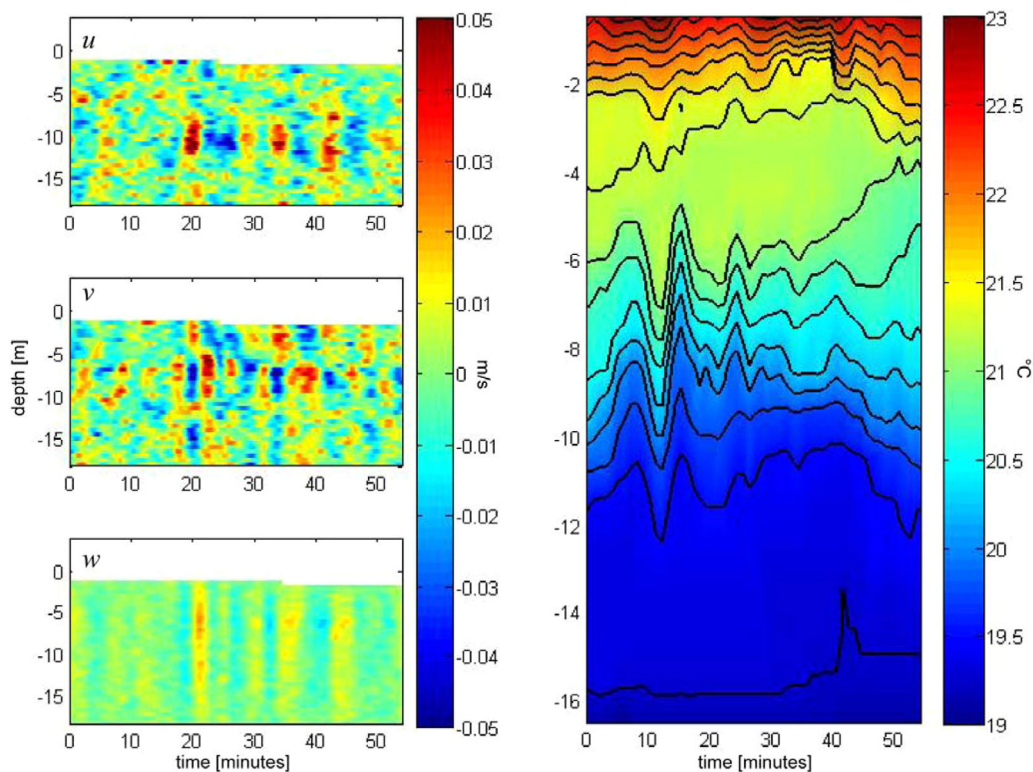


Figure 10. Comparison of observations of (left-hand plots) an internal wave flood event observed in the EXPOL ADCP record and (right-hand plot) the contemporaneous observations at the Hobo thermistor string. The three plots in the left-hand column show the band-passed u , v , and w velocities (color scale: $\pm 0.05 \text{ m s}^{-1}$) by depth (meters, ordinate axes) and time (minutes, abscissa axes) from the EXPOL ADCP record. The right-hand plot shows temperatures (contours at 0.25°C) from the Hobo thermistor string for the same depths and times. The 0 min time is 15:17 GMT on 11 August 2009.

The mean shear-squared and mean gradient Richardson number results presented in section 3.1 were derived from velocity records that were filtered using a 20 min cutoff in order that the records from ADCP1 and EXPOL could be directly compared. This filtering also removed any increased shear due to internal waves at periods below 20 min. The internal wave activity seen in the 2–20 min band-pass filtered records of EXPOL shown in Figure 10 clearly contains vertical shear at frequencies above 20 min periods. It is worthwhile to compare S^2 and Ri estimates from EXPOL that include this additional shear with those presented in section 3.1. Figure 11 shows a comparison of the estimates (above the noise) of the mean depth-averaged shear-squared and gradient Richardson numbers computed from the EXPOL record using the 20 min low-pass filtering (blue) presented earlier with those using a 2 min low-pass filtering (red). The 2 min filtering includes shear due to internal waves whereas the 20 min filtering excludes this. Figures 11e and 11f show that after midflood there is an increase in S^2 and a decrease in Ri within the pycnocline when shear in the 2–20 min period frequency range is included in the estimation. This is consistent with Figure 7, which showed that the period after midflood is when the near-bottom internal wave activity is the highest. Note that the inclusion or exclusion of the 2–20 min frequency range had no impact on the calculation of the tidal evolution of buoyancy frequencies shown in Figure 4: the changes in Ri seen in Figure 11f are therefore due to the additional shear present in the 2–20 min period frequency range.

3.4. Tidal Cycles of Near-Bottom Temperature, DO, and Salinity

The concurrent records at the nearby EXRK buoy allow an evaluation of the tidal evolution of the near-bottom tendencies ($\partial/\partial t$) of heat, DO, and salt. Figure 12 shows the tidally phase-averaged tendencies of DO, temperature, and salinity at the near-bottom sensor package of the EXRK buoy during the 16 days of the ADCPs and thermistor chain deployment. It is apparent that there are substantial increases in both DO and temperature that occur during the flood tide accompanied by a concurrent decrease in salinity. Also shown by the dashed red line in the temperature plot are the temperature tendencies recorded by the bottom thermistor of the Hobo chain. Because the thermistor chain was NNE of the EXRK buoy by

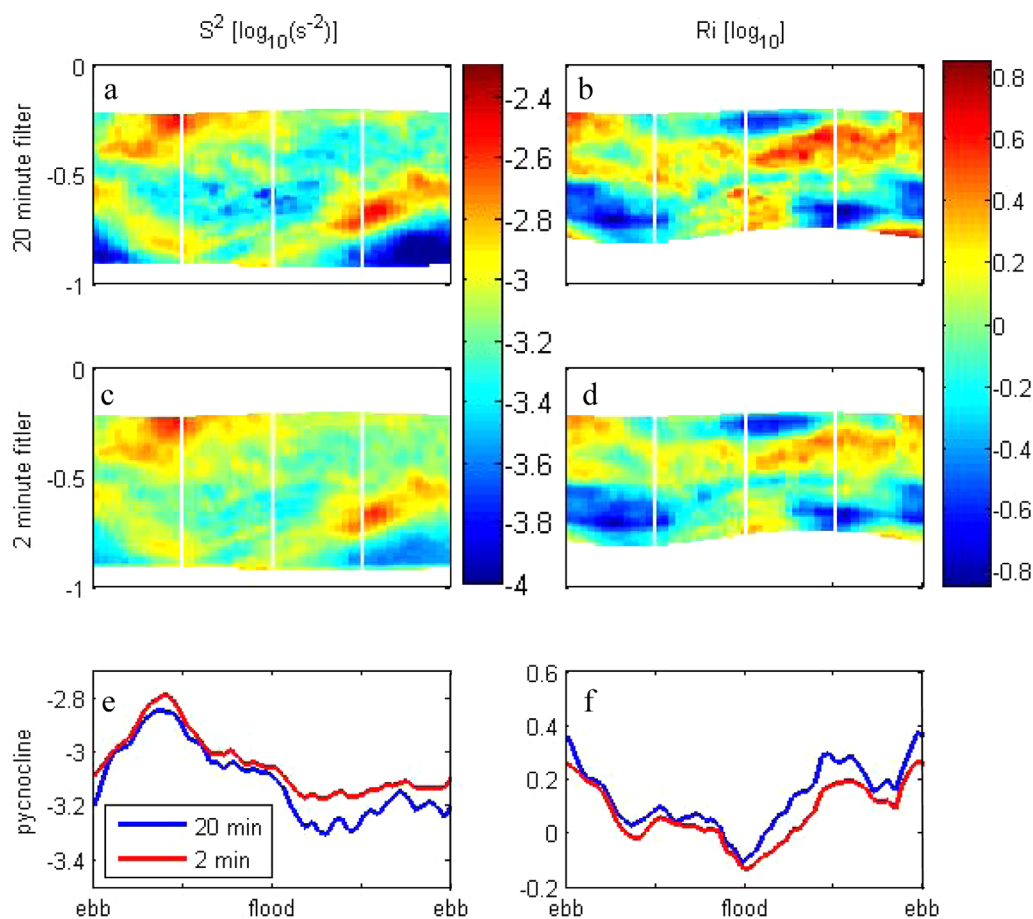


Figure 11. Comparison of the phase-averaged \log_{10} shear-squared (a, c, e), and gradient Richardson numbers (b, d, f) using proxy densities from the thermistor chain and velocity records from EXPOL that were filtered using a 20 min low-pass cutoff period (a, b; blue) and that were filtered using a 2 min low-pass cutoff period (c,d; red). The bottom plots show the depth-averaged pycnocline means ($-0.50 \leq \sigma \leq -0.22$).

approximately 525 m (see Figure 1), these would be expected to lead the EXRK measurements during the flood as is seen in Figure 12c.

Figure 13a shows the mean tidal evolution of the depth structure of temperature tendencies observed at the thermistor string. It is evident that the near-bottom increases in temperature observed during the flood at the EXRK buoy and shown in Figure 12c occur contemporaneously throughout the water column. Figure 13b shows the evolution of isotherms during the mean tidal cycle, clearly indicating a coherent mean depression of the thermocline of about 4 m occurring during the flood. The tidal phase averages of the proxy densities calculated using the thermistor temperatures in conjunction with the temperature and salinity relationship ($r=0.92$) observed in the buoy records are shown in Figure 13c.

The midflood mean pycnocline depression seen in Figure 13c appears to be a fairly robust feature at the EXRK location but a similar depression does not appear to occur throughout all of the WLIS. Figure 14 shows the tidally phase-averaged near-bottom tendencies of temperature and DO at the EXRK and the 7.7 km distant FB02 buoys from 2005 (see Figure 1 for locations). Figure 14 shows that the pattern of near-bottom tendencies of temperature and DO observed in 2009 and shown in Figure 12 is also seen in the 2005 EXRK buoy records, indicating that at EXRK this phenomenon may occur most years. The record at the FB02 buoy shows an entirely different tidal pattern, however. The differences between the EXRK and FB02 buoys indicate that the phenomenon observed near EXRK may be spatially variable over distances of only a few kilometers.

A clearer picture of both the tidal and subtidal evolution of temperature, salinity, and DO is seen by demodulating the records at the M_2 frequency. Demodulation at the M_2 frequency preserves discrete data points,

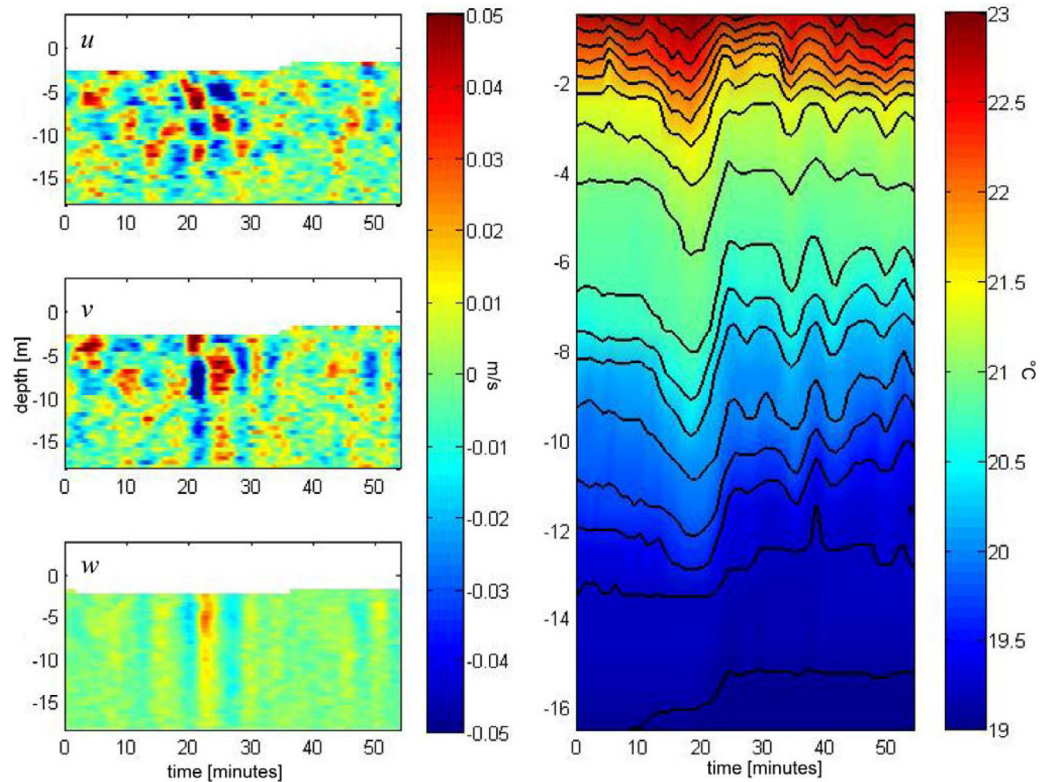


Figure 12. Phase-averaged near-bottom tendencies ($\partial/\partial t$) of (a) DO ($\mu\text{M d}^{-1}$), (b) salt (PSU d^{-1}), and (c) temperature ($^{\circ}\text{C d}^{-1}$) at the EXRK buoy (NOAA 44022) during the 16 day deployment. The abscissa shows the M_2 tidal phase. The shaded areas show ± 1 standard deviation. Also shown in Figure 12c in black/gray are the phase-averaged temperature tendencies of the bottom sensor of the Hobo thermistor chain located 525 m NNE of the EXRK buoy. The horizontal labels “ebb” and “flood” represent maximum near-bottom ebb and flood at the M_2 frequency at ADCP1.

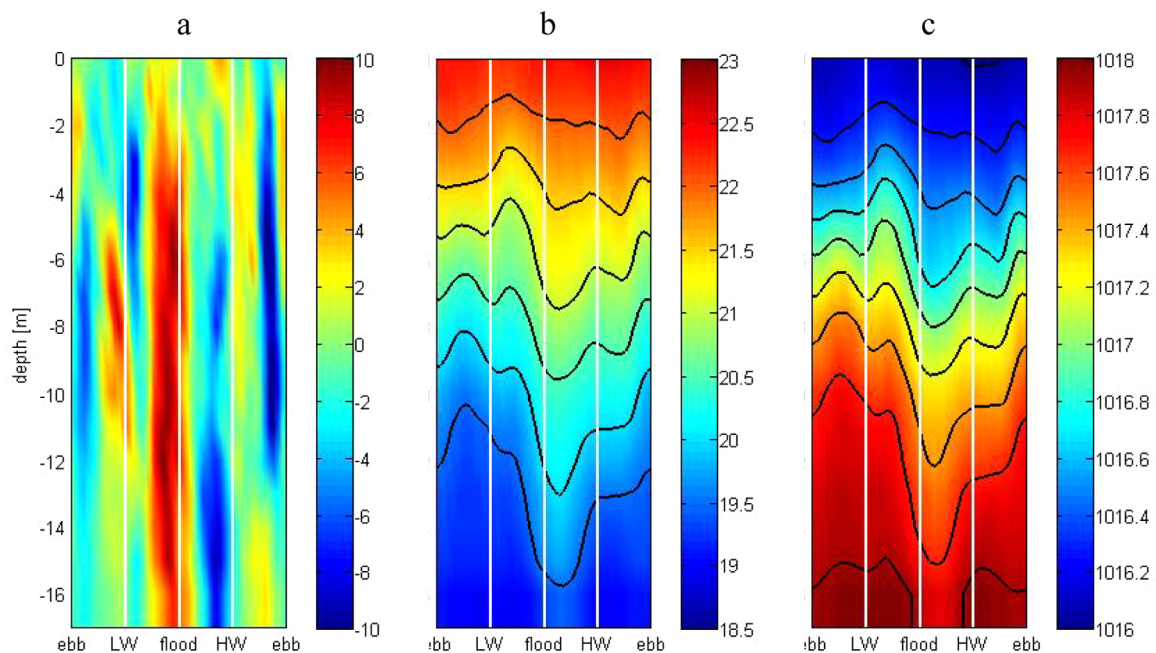


Figure 13. (a) Phase-averaged temperature tendencies from the Hobo thermistor string ($^{\circ}\text{C d}^{-1}$); (b) tidally phase-averaged temperatures (contours at 0.5°C) showing the evolution of the thermocline during a tidal cycle; (c) Isopycnals (contours at 0.25 kg m^{-3}) during a tidal cycle using proxy densities calculated from the thermistor temperatures. Depths are depths below the free surface at $H + \eta$. The horizontal labels “ebb” and “flood” represent maximum near-bottom ebb and flood at the M_2 frequency at ADCP1.

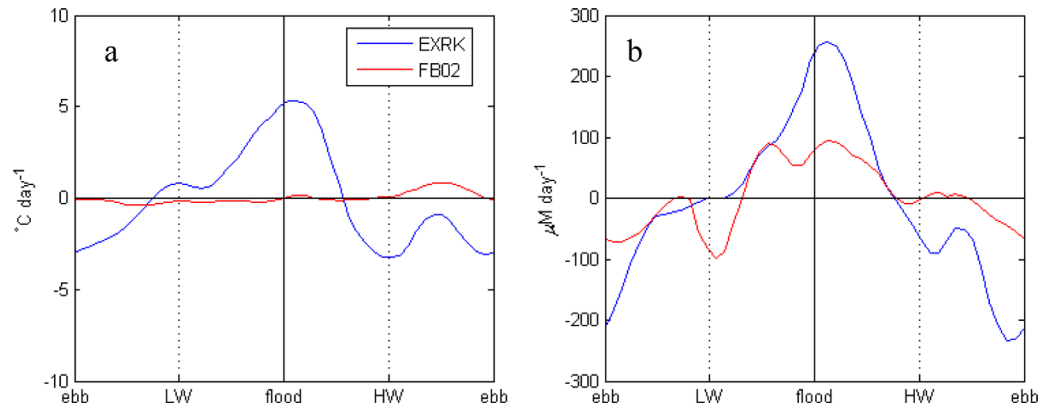


Figure 14. (a) Phase-averaged near-bottom tendencies of temperature ($^{\circ}\text{C d}^{-1}$), and (b) DO ($\mu\text{M d}^{-1}$) for 2005 at the EXRK (blue) and FB02 (red) buoys.

but “lines up” each tidal cycle on top of the previous so that the x axis shows tidal variability and the y axis shows subtidal variability. See Appendix A for more information on the demodulation and phase-averaging methods we employed. Figure 15 shows a comparison of the demodulation of the near-bottom internal wave activity observed at the Hobo thermistor chain during the 16 day deployment with demodulations of the near-bottom temperature, salinity, and DO tendencies. Figure 15 shows significant correlations ($p < 0.01$) between the near-bottom internal wave activity and the near-bottom evolution of temperature, heat, and DO. At subtidal scales, stronger periods of both IW energy and scalar tendencies occur during days 1–3, days 6–9, and days 10–12. There is also a clear correspondence between the timing of these events and the variability in the apparent phase of the M_2 tide due to the interaction of the M_2 with the N_2 and S_2 as shown by the white lines in Figure 15 and discussed in Appendix A. Note that there is substantial

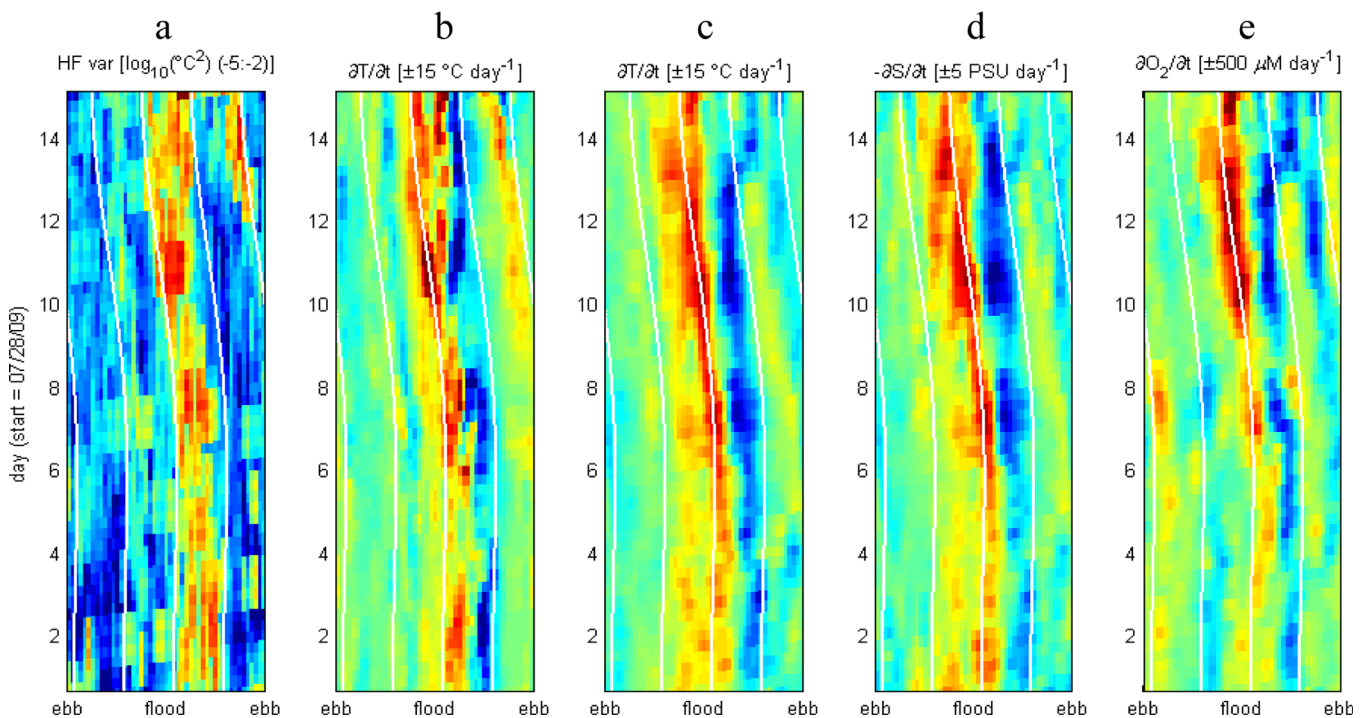


Figure 15. Demodulation by M_2 tidal phase (abscissa axes) over the 16 day deployment (ordinate axis). (a) The near-bottom internal wave spectral energy as the \log_{10} (color range: -6 to -2) of the high-passed variance ($^{\circ}\text{C}^2$) at the near-bottom sensor of the Hobo thermistor array; (b) The low-passed 1 h tendencies ($f = 3 \cdot 10^{-4}\text{Hz}$) of the same near-bottom record from the thermistor chain ($\pm 15^{\circ}\text{C d}^{-1}$); (c, d, e) show the 1 h near-bottom tendencies of (c) temperature ($\pm 15^{\circ}\text{C d}^{-1}$), (d) salt ($\pm 5 \text{ PSU d}^{-1}$), and (e) DO ($\pm 500 \mu\text{M d}^{-1}$) from the EXRK buoy. (d) The salt tendency as $-\partial S/\partial t$ so that it can be better compared with the other plots. The white lines show the expected variation in the timing of the semidiurnal tide due to the M_2 - S_2 spring-neap and the M_2 - N_2 monthly cycles as discussed in Appendix A.

IW activity during the ebb after day 12 that is reflected in the collocated thermistor tendencies (Figure 15b) but that is not seen in the near-bottom buoy tendencies shown in Figures 15c–15e.

4. Discussion

The subtidal variability in Ri and the subtidal DO and heat tendencies show low correlation over the 2 week deployment. The longer buoy records from 2005 [see *McCardell and O'Donnell*, 2014] show some correlation between Ri (estimated using the near-surface to near-bottom density differences and the depth-averaged shear squared from contemporaneous ADCP deployments described by *Bennett et al.* [2010]) and near-bottom DO and heat tendencies, but only at the seasonal scale. In the WLIS region, where the longitudinal salinity gradients are approximately $\partial S/\partial x = 6 \cdot 10^{-5}$ PSU m^{-1} (see Table 3.1), typical depths are $H=20$ m, maximum near-bottom velocities are 20 cm s^{-1} implying a friction velocity in the BBL of order $u_* \cong \sqrt{C_d U_{1m}^2} = 1$ cm s^{-1} where $C_d \sim 0.0025$ is the drag coefficient, and U_{1m} is the velocity magnitude at $-H+1$ m, the Simpson number, Ri_x is of order 2 or greater. This is well above the critical Ri_x value of 0.1 suggested by *McCready and Geyer* [2010] or the higher value of 0.2 suggested by *Li et al.* [2007], indicating that periodic mixing due to tidally strain-induced destratification is unlikely. Currents in the western end of LIS are too low for significant tidal straining to occur.

In the WLIS near EXRK, the tidal currents also seem insufficient to create the degree of BBL growth observed by *Chant et al.* [2007]. *Chant et al.* observed near-surface currents greater than 1 m s^{-1} and near-bottom currents on the order of 0.5 m s^{-1} in the Hudson River; in the WLIS near EXRK, maximum surface currents are generally less than 0.25 m s^{-1} and near-bottom currents are less than 0.20 m s^{-1} [*Bennett et al.*, 2010; also see Figure 3]. The depths in the Hudson River region *Chant et al.* studied (8–15 m) are also shallower than those in the WLIS near EXRK (17–23 m). Given the considerably lower velocities in the WLIS and the greater water column depth, one would expect the relative thickness of the BBL to be considerably less than that observed in the Hudson. Whereas *Chant et al.* [2007] observed BBL thicknesses ranging from somewhat greater than 50% the water column depth during neap tides to greater than 75% the water column depth during spring tides, the results from the ADCP1 estimates we made indicate that in the vicinity of EXRK in the WLIS, the maximum BBL thickness is generally less than 25% of the water column depth. Without any other processes, this would indicate that BBL entrainment of pycnocline water is unlikely to be an important mixing mechanism in the WLIS on its own.

Figure 12 shows that there are substantial increases in near-bottom DO and temperature and a commensurate decrease in salinity that occur midflood. These are not the changes that would be expected due to advection of along-Sound gradients by the tide. Using positive x as the out-of-Sound direction (east), the observations described in *McCardell and O'Donnell* [2014] indicate that during mid-summer, $\partial[O_2]/\partial x > 0$, $\partial T/\partial x < 0$, and $\partial S/\partial x > 0$, so that advection by the flood ($u < 0$) would be expected to result in $\partial[O_2]/\partial t > 0$, $\partial T/\partial t < 0$, and $\partial S/\partial t > 0$. Although an increase in DO is seen during the flood, the decrease in temperature and increase in salinity that would be expected due to advection by the flood tide are not observed in Figure 12. Midflood increases in DO and temperatures and decreases in salinity are, however, what would be expected due to vertical processes. At EXRK, warmer, fresher, and oxygen richer surface waters overlie the bottom waters. Downward advection or vertical mixing would therefore be expected to result in an increase in DO, an increase in temperature, and a decrease in salinity. This is exactly what is seen in the observations of near-bottom tendencies during the flood shown in Figure 12, indicating that near-bottom changes occurring during the flood are the result of vertical processes. Additionally, since the maximum near-bottom horizontal currents at EXRK observed during the flood are only approximately 20 cm s^{-1} (see Figure 3), the horizontal gradients that would be required to create the near-bottom DO tendencies of greater than 200 μM d^{-1} during midflood seen in Figure 13 would need to exceed 10 μM km^{-1} . This is an order of magnitude greater than the observed along-Sound gradients observed by *McCardell and O'Donnell* [2014] of 2 ± 2 μM km^{-1} at the nearby FB02 buoy and is further evidence that the increases in near-bottom DO during the flood tide are not the result of along-Sound advection.

The observed increases in DO and temperatures and decreases in salinity that occur during mid-flood are due to mid-flood depressions of the oxycline, thermocline, and halocline. Figure 4a shows that the pycnocline (as defined by the level of the maximum density gradient and seen in Figure 4a as the N^2 maxima) drops and weakens midway through the flood. As seen in Figure 13c, this drop in the pycnocline is

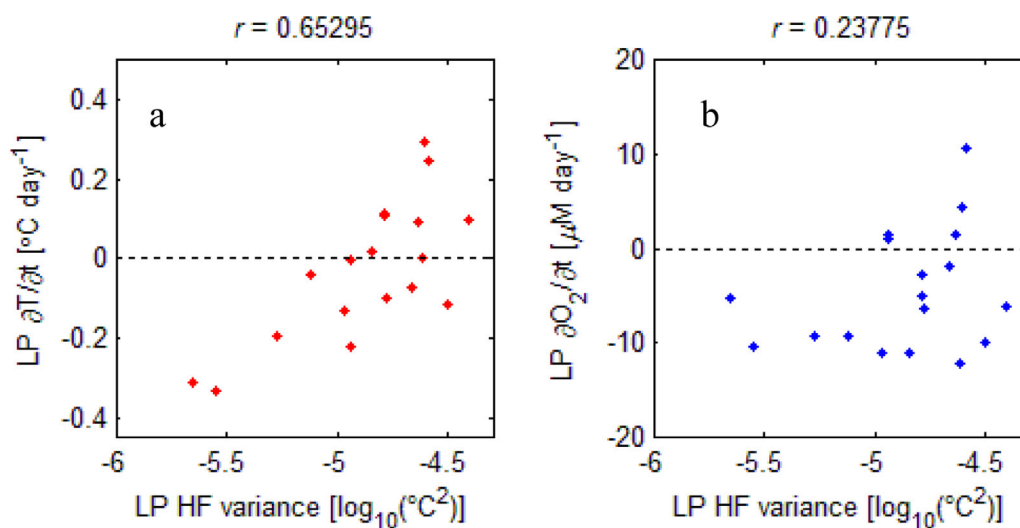


Figure 16. Correlations between the 20 h mean near-bottom internal wave spectral energy ($\log_{10}^{\circ}\text{C}^2$) at 2–20 min periods determined as the low-passed ($f=1.4 \cdot 10^{-5}$ Hz) mean of the high-passed ($8 \cdot 10^{-4}$ Hz) variance from the bottom sensor of the Hobo thermistor chain with the 20 h low-passed ($f=1.4 \cdot 10^{-5}$ Hz) means of the near-bottom temperature tendencies (a, $^{\circ}\text{C d}^{-1}$) and DO tendencies (b, $\mu\text{M d}^{-1}$).

accompanied by a comensurate (5 m) mean depression of isopycnals throughout the water column. Note that Figure 13c is only showing the mean pycnocline depression caused by these events. The estimations of the maximum internal thermocline depressions shown in Figure 9 indicate individual IW depressions are up to 10 m.

Figure 9 also shows that there is a positive correlation between the maximum internal wave amplitudes and the net near-bottom temperature change during a tidal period. Figure 15 shows that there is also substantial correlation between the degree of internal wave activity and the magnitudes of the near-bottom tendencies. If increased mixing is also occurring as the result of internal wave activity, there should also be a correlation between the subtidal variability in internal wave activity and the subtidal near-bottom tendencies: Figure 16 shows the correlation between the 20 h low-passed near-bottom wave spectral energy (as indicated by the temperature variance at IW frequencies shown in Figure 15a) with 20 h low-passed near-bottom tendencies of temperature (Figure 15a) and DO (Figure 15b). Although the subtidal tendencies of both DO and temperature show positive correlations with the near-bottom internal wave energy, only the temperature tendency correlation is significant at a 95% confidence level. Although we report the correlation coefficients, one would not expect linear relationships. For example, as vertical mixing is reduced, DO tendencies would be expected to approach the net of biological demand and horizontal resupply. *McCardell and O'Donnell* [2014] estimate this net loss would be $-16 \pm 10 \mu\text{M d}^{-1}$, which is consistent with DO tendencies during periods of low internal wave activity as shown in Figure 16. At subtidal scales, other mechanisms, such as the variability in the along-Sound wind stress observed by *O'Donnell et al.* [2008], may be involved as well.

Mixing that occurs due to internal waves is usually thought to be the result of either internal wave breaking or enhanced shear [*Burchard, 2002*]. Figure 11 indicates that when the additional shear from motions at internal wave frequencies is included in our shear estimations, there are increases in shear squared and reductions in *Ri* estimates, particularly after midflood. If the variability in this additional shear is compared with near-bottom tendencies at subtidal scales in a manner similar to that of Figure 16, only a weak correlation ($r = 0.30$, $p = 0.05$) is observed. This suggests that although increases in shear due to internal waves clearly reduce mean *Ri* estimates, other mechanisms may be responsible for the correlation between the variability in internal wave amplitudes and near-bottom net tidal temperature changes ($r = 0.54$, $p = 0.001$, see Figure 9) and the correlation between variability in the near-bottom internal wave spectral energy and the near-bottom tendencies ($r = 0.65$, $p = 0.00005$, see Figure 16).

An increase in mixing due to internal wave activity could also occur if the internal wave motion brings a water mass with increased vertical concentration gradients (i.e., the thermocline, halocline, or oxycline) into or near the bottom boundary layer. *Chant et al.* [2007] observed a BBL that grew to a sufficient height to entrain pycnocline water; a sufficient descent of the pycnocline into the BBL would also result in

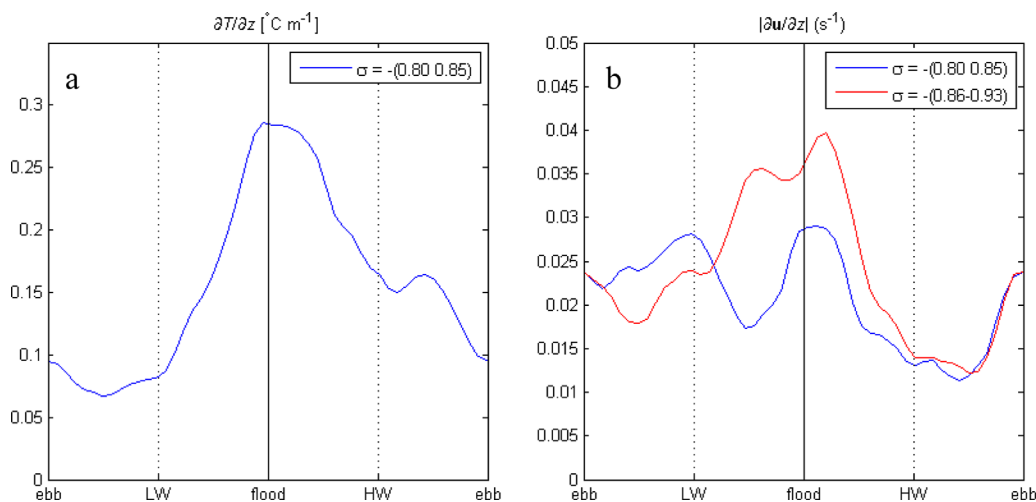


Figure 17. Comparison of the tidal evolution of (a) near-bottom vertical temperature gradients, $\partial T/\partial z$ ($^{\circ}\text{C m}^{-1}$) with (b) near-bottom shear, $|\partial u/\partial z|$, (s^{-1}). Since the thermistor sensors move up and down tidally relative to the bottom, (a) The results in σ (bottom-following) coordinates for σ levels between -0.85 and -0.80 . These represent the deepest above-bottom depths that were continuously sampled by the thermistor chain during the tidal cycles. (b) The tidal evolution of the near-bottom shear from the ADCP1 record at the same σ depths as Figure 17a in blue. Also shown in Figure 17b in red is the shear for σ levels between -0.93 and -0.86 which represent the deepest depths sampled by ADCP1.

entrainment of pycnocline water by the BBL. When fluxes due to vertical mixing are modeled as $K_v \partial C/\partial z$ where K_v is a vertical eddy diffusivity and $\partial C/\partial z$ is a concentration gradient, mixing will increase if either K_v or $\partial C/\partial z$ is increased. Figure 17 shows the tidal evolution of the near-bottom vertical gradients of temperature at the Hobo thermistor chain and the near-bottom shear at ADCP1. Figure 17a indicates that the near-bottom vertical temperature gradients increase by a factor of four during midflood. Since the entire water mass is moved downward by the internal tide, salinity, and DO gradients would be expected to show similar increases during the flood. Figure 17b shows that the near-bottom shear during a tidal cycle is also maximal during or near the midflood. It is clear from Figure 17 that periods of maximum near-bottom gradients resulting from the midflood depressions of the pycnocline coincide with periods of maximum near-bottom shear resulting from the growth of the BBL during the flood.

The subtidal near-bottom temperature tendencies show warming about half of the time and cooling about half of the time (see Figures 2d, 6a, 9b, and 16a). Since periods of bottom water warming may result from periods of increased mixing, it is worthwhile to compare the near-bottom tidal tendencies during periods of near-bottom warming with those during periods of near-bottom cooling. Figure 18 shows a comparison of the tidal evolution of near-bottom temperature and DO tendencies during cooling and warming regimes. Figure 18 indicates that during warming periods, the midflood increases in both temperature and DO are considerably greater than during cooling periods. The greater mid-flood tendencies indicate that the internal tide is deeper and internal waves are more pronounced during this time. This is consistent with the subtidal correlation seen in Figure 9 between the net near-bottom temperature changes and maximum internal wave depressions.

Greater internal activity during periods of subtidal increases in temperature is also evidenced in the unfiltered buoy records of near-bottom DO and temperature that were shown in Figures 2c and 2d. During the second half of the deployment, where near-bottom temperatures are increasing and the near-bottom DO decline is arrested, the magnitude of variability at the 15 min buoy sampling period is noticeably greater, particularly for DO. Toward the end of the record, periods of what appear to be “noise” in both the temperature and DO records are likely due to aliasing of internal waves with the 15 min buoy sampling interval.

If mixing occurs during the midflood as a result of internal waves, then this should be evidenced not only by the near-bottom tendencies, but throughout other portions of the water column. Figure 13c shows spreading of isopycnals occurs throughout the water column during the flood, which is indicative of diapycnal mixing. Cross-pycnocline mixing should also result in a reduction of vertical gradients in the pycnocline. Figure 19 shows a comparison between the tidal evolution of N^2 during periods of (Figure 19a) cooling and

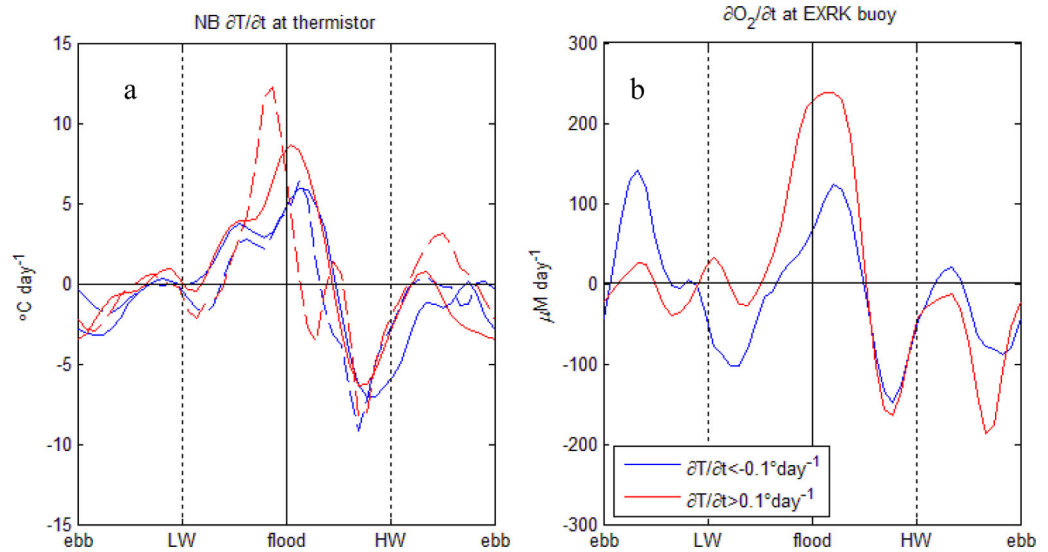


Figure 18. Comparison of the tidal phase-averages of near-bottom (a) temperature ($^{\circ}\text{C d}^{-1}$) and (b) oxygen tendencies ($\mu\text{M d}^{-1}$) during (blue) cooling ($\langle \partial T/\partial t \rangle < -0.1^{\circ}\text{C d}^{-1}$) and (red) warming ($\langle \partial T/\partial t \rangle > 0.1^{\circ}\text{C d}^{-1}$) periods. The solid lines show the near-bottom tendencies at the EXRK buoy, the dashed lines in Figure 18a show the near-bottom temperature tendencies at the lowest sensor of the thermistor string. Compare to Figures 2 and 14.

(Figure 19b) warming. Figure 19 shows evidence that during periods of warming, presumably associated with increased vertical mixing, there is a greater breakdown in the pycnocline that occurs during the mid-flood and a greater reduction in buoyancy frequencies after midflood. The depression of the remaining pycnocline is also more pronounced during the warming periods. Deeper midflood pycnocline depressions during warming periods are also evidenced by the estimations of the maximum internal wave depressions per tide shown in Figure 9a. The greater reduction in the pycnocline gradients that is observed during warming periods shown in Figure 19b is further evidence that cross-pycnocline mixing is occurring. Figure 19 also indicates that the tidal cycle of stratification shown earlier in Figure 4a and Figure 5e, with minimum buoyancy frequencies within the pycnocline occurring during the flood, may be the result of—as opposed to the cause of—mixing.

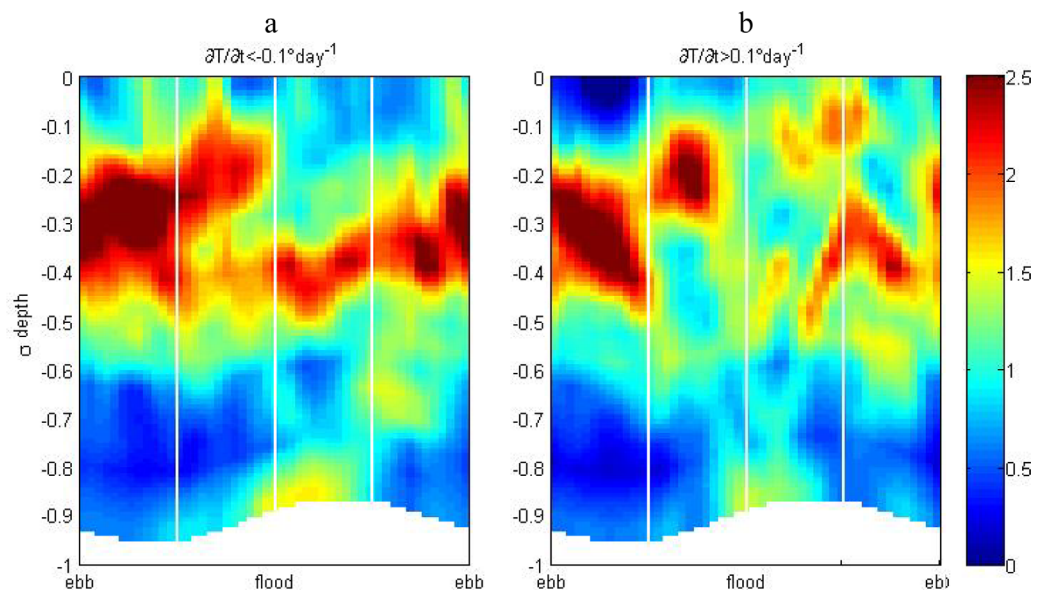


Figure 19. Tidal phase averages of the buoyancy frequency squared, ($\text{s}^{-2} \cdot 10^{-3}$) during (a) cooling ($\langle \partial T/\partial t \rangle < -0.1^{\circ}\text{C d}^{-1}$) and (b) warming ($\langle \partial T/\partial t \rangle > 0.1^{\circ}\text{C d}^{-1}$) periods by tidal phase and sigma depth. The horizontal labels “ebb” and “flood” represent maximum near-bottom ebb and flood at the M_2 frequency at ADCP1.

5. Conclusions

Because the currents in the WLIS are weak, it seems unlikely that either tidally driven periodic destratification or BBL entrainment are significant vertical mixing mechanisms on their own. Within the pycnocline, the tidal cycle of Ri suggests that maximum vertical mixing occurs during the midflood. The timing of the minimum Ri within the pycnocline is coincident with a tidal cycle of internal waves that creates a strong pycnocline depression at midflood. Depression of near-surface waters during the midflood results in near-bottom heat and DO increases and salinity decreases as warmer, more oxygenated, and fresher waters are brought downward. The depression of isopycnals also results in significant increases in near-bottom vertical gradients that are coincident with regions of increased shear due to BBL growth during the flood. This depression creates the possibility of entrainment of pycnocline waters by the BBL despite low tidal velocities resulting in maximum BBL heights of only 25% the water column depth.

Evidence that an increase in vertical mixing is associated with these internal transport events is seen in the correlation of near-bottom subtidal tendencies with near-bottom internal wave activity. During near-bottom warming periods, which are presumably associated with periods of increased vertical mixing causing ventilation of the bottom waters, the amplitude and near-bottom spectral energy of internal waves that occur during midflood is greater, mean pycnocline depressions are deeper, a greater breakdown in stratification occurs during the flood, and the reestablishment of the pycnocline is weaker. These observations imply that, during the summertime period of thermal stratification in the WLIS region near Execution Rocks, modulation of vertical transport by internal waves is an important mechanism.

Appendix A: Phase Averaging Methodology

This appendix describes the phase-averaging methodology used. Defining the phase, φ , at frequency ω as:

$$\varphi(t) = \text{rem}(\omega t - \phi_0, 2\pi) \quad (\text{A1a})$$

where $\text{rem}(a, b) \equiv a - b|a/b|$ is the remainder after division and ϕ_0 is a constant representing the zero reference phase. Using $\varphi(t)$ from equation ((A1a)a), the phase-average, u_{PA1} , at frequency ω is:

$$u_{PA1}(\varphi) = \overline{u(\varphi(t))} \quad (\text{A2a})$$

For discrete data sets, the resolution of φ is dependent on the $u(t)$ sampling interval, and the size of the phase interval should be chosen such that $u(\varphi(t))$ includes data from each cycle of $u(t)$ at frequency ω or aliasing can occur. This problem can be lessened by sub sampling $u(t)$ prior to phase-averaging.

Using τ to represent a long-time dimension, the demodulation, u_{DM1} , at frequency ω is:

$$u_{DM1}(\varphi, \tau) = \overline{u(\varphi(t))} \quad ||t - \tau| \leq \varepsilon \quad (\text{A3a})$$

where 2ε is the window size in the τ dimension. For the demodulations presented herein, $\varepsilon = 2.5 \cdot \pi/M_2$ was used. This represents a $2^{1/2}$ tidal cycle or 31 h window.

We now consider phase-averaging and demodulation that is identical to A2a and A3a except that the zero reference phase, ϕ_0 , of equation (A1a) is allowed to vary slowly (compared to ω^{-1}) as a function of t :

$$\varphi_b(t) = \text{rem}(\omega t - \phi(t), 2\pi) \quad (\text{A1b})$$

$$u_{PA2}(\varphi_b) = \overline{u(\varphi_b(t))} \quad (\text{A2b})$$

$$u_{DM2}(\varphi_b, \tau) = \overline{u(\varphi_b(t))} \quad ||t - \tau| \leq \varepsilon \quad (\text{A3b})$$

By allowing the zero reference phase, ϕ , to vary, fortnightly and monthly variability in the timing of the semidiurnal tide can be included in the phase-average and the demodulation. This variability in apparent phase is clearly seen in demodulations of the tidal velocities. Figure A1 shows a comparison of the near-bottom along-channel and across-channel velocities at ADCP1 demodulated at the M_2 frequency according to equation ((A3a)a) with those demodulated according to equation ((A3a)b) by using a sinusoidal function of $M_2 - b_2$ and $M_2 - a_2$ frequencies for $\phi(t)$. The coefficients for the $\phi(t)$ function used were determined by harmonic analysis of the along-channel component of the near-bottom ADCP1 record. Lines representing the function of ϕ that was used are shown as $\phi(\tau + n \cdot \pi/2)$, $n = 0 : 4$, in the plots of the demodulations of

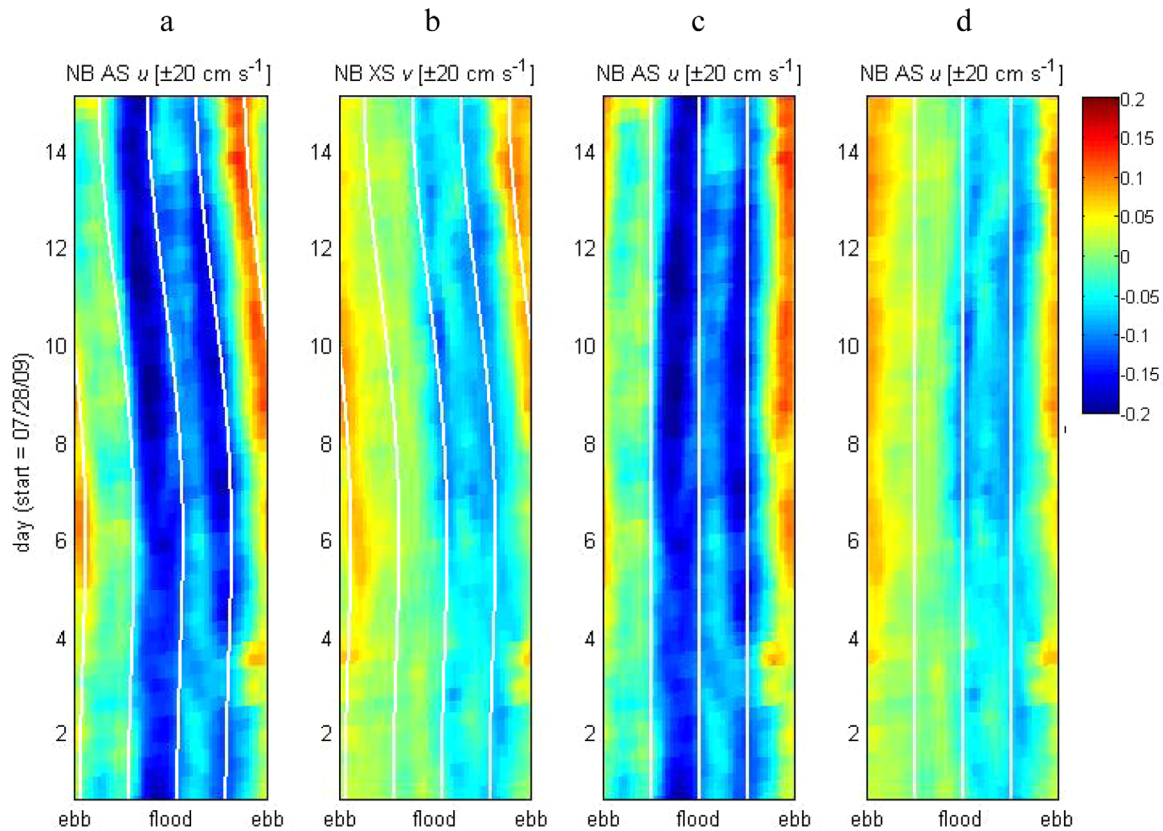


Figure A1. Comparisons of tidally demodulated plots of the (a, c) near-bottom along-channel and (b, d) cross-channel velocities using the (a, b) “plain” demodulation of equation (A3a) (Figures A1a and A1b) and using the “enhanced” methodology of equation (A3b) where the phase of the primary semidiurnal tide is corrected for fortnightly and monthly variability (Figures A1c and A1d). Shown in white in Figures A1a and A1b is the variability of the primary tidal phase at the $M_2 - \omega_2$ and $M_2 - a_2$ frequencies as determined by a harmonic analysis of the ADCP1 record. These lines are “straightened” out by the methodology of equation (A3b) shown in Figures A1c and A1d.

Figures A1a and A1b. These lines show the best least-squares fit of the $S_2 - M_2$ and $N_2 - M_2$ frequencies to the variability in the phase of the primary semidiurnal tide ($r^2 = 0.76$). These become straight lines in the plots of Figures A1c and A1d which include this variability in the demodulation.

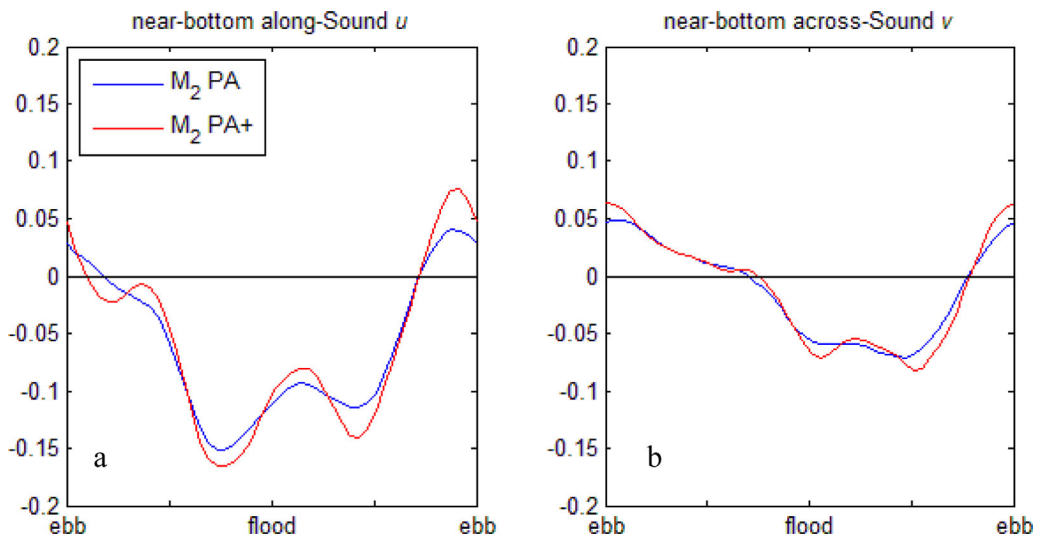


Figure A2. Comparison of the tidally phase-averaged near-bottom (a) along-Sound and (b) across-Sound velocities ($m s^{-1}$) at ADCP1 (blue lines) using the methodology of equation (A2a) with those estimated using equation (A2b). The blue plots also represent the averages along the ordinate direction of the two left-hand plots of Figure A2 whereas the red plots represent ordinate averages of the right-hand plots of Figure A1.

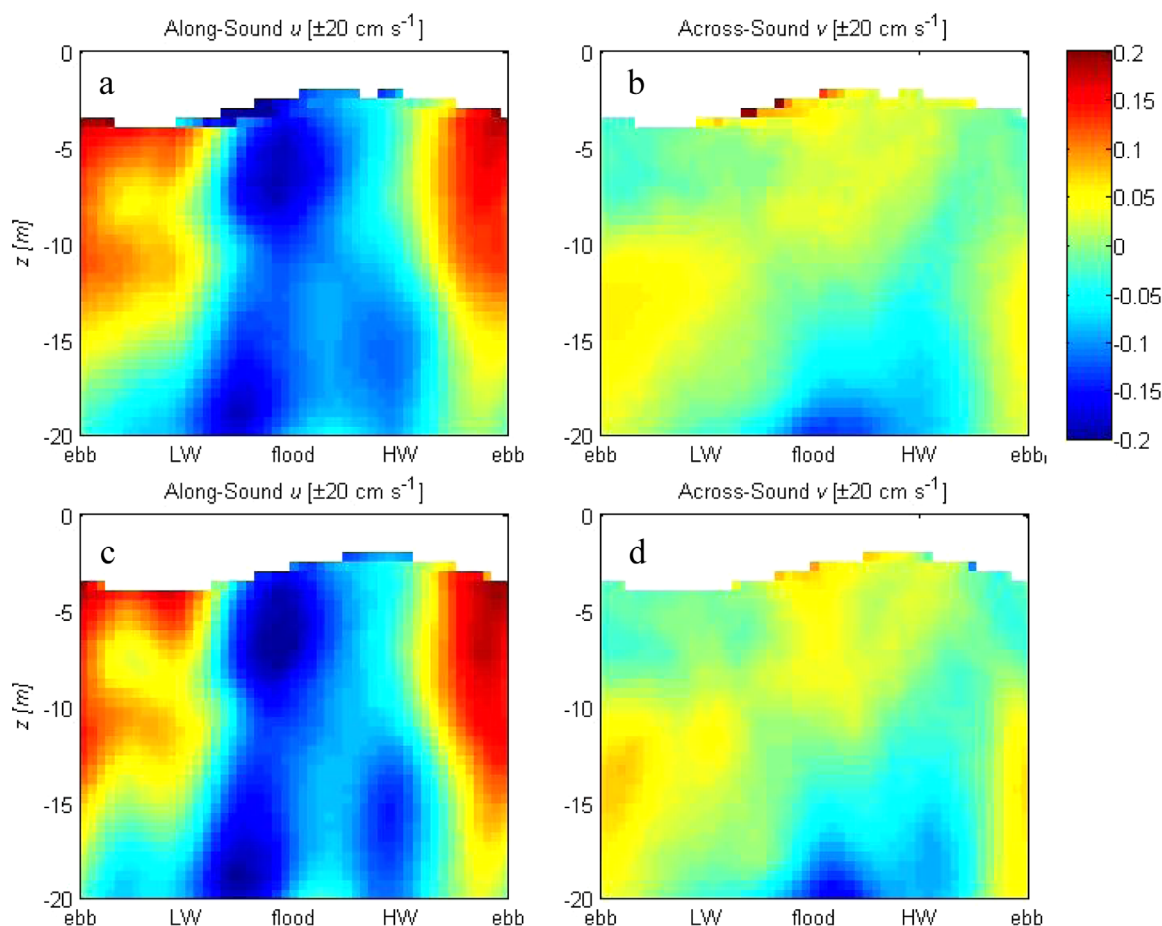


Figure A3. (left-hand: a, c) Along-Sound and (right-hand: b, d) across-Sound tidal velocity structures determined through plain (top a, b) phase-averaging at the M_2 frequency and (bottom c, d) the phase-averaging methodology that includes fortnightly and monthly variability in the phases of the semidiurnal tides. All four plots show the tidal structure by depths (ordinate axes, m) and tidal phase (abscissa axes). All four plots use a color range of $\pm 0.2 \text{ cm s}^{-1}$ and 56° east of north was used as the along-Sound axis with positive u being an ebb flow in this direction: this corresponds with the near-bottom major axis at EXRK reported by Bennett *et al.* [2010].

Figure A2 shows a comparison of the “normal” phase-averaging of equation (A2a) (blue) with the “enhanced” phase-averaging of equation (A2a) (red). Since averaging the τ dimension of equations (A3a) and (A3b) will yield phase-averages that are equivalent to the results given by equations (A2a) and (A2b), the results shown in Figure A2 can also be considered as representing the τ averages of the results shown in Figure A1; i.e., the results shown in blue in Figure A2 represent averages along the long-time dimension of the left-hand plots of Figure A1 while the results shown in red represent averages of the right-hand plots.

Figure A3 shows a similar comparison to that of Figure A2 for the entire water column. As is seen in Figures A2 and A3, removing the variability at the fortnightly and monthly frequencies before averaging the demodulation in the long time scale dimension allows for a more detailed and less “blurred” picture of the mean tidal structures.

Although the differences shown in Figures A2 and A3 are subtle, note that the amplitudes of the semidiurnal tide are better resolved in the plots using the “enhanced” methodology, and that those of the M_6 harmonic are significantly better resolved. There is also considerably more detail resolved using the “enhanced” methodology. The variance remaining after filtering using the “enhanced” methodology is also significantly greater: for the along-channel u , this increases from $r^2=0.61$ for the “plain” phase-averaging to $r^2=0.81$ for the “enhanced” phase-averaging with an F-test significance of at least $1 - 0.0007$. Although the across-channel flow, v , was not included in the estimation of $\phi(t)$, this shows a similar increase from $r^2=0.62$ to $r^2=0.80$.

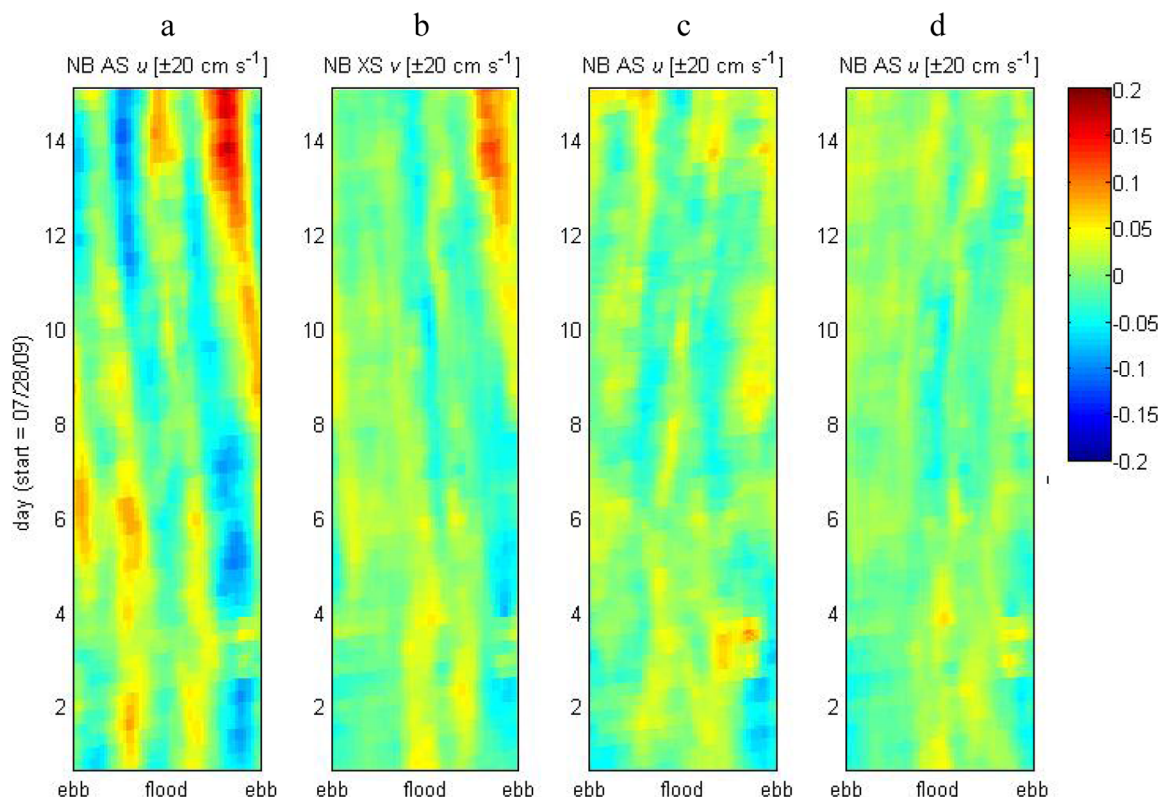


Figure A4. Comparisons of demodulated plots of the residuals of the tidally phase-averaged near-bottom (a, c) along-Sound and (b, d) cross-Sound near-bottom velocities (m s^{-1}) at ADCP1 using (Figures A4a and A4b) the “normal” phase-averaging methodology of equation (A2a) with (Figures A4c and A4d) those estimated using the “enhanced” methodology of equation (A2b).

Figure A4 shows a comparison of the residuals after the “normal” phase-averaging of equation ((A2a)a) (left-hand plots) with those remaining after the “enhanced” phase-averaging of equation ((A2a)b) (right-hand plots). As indicated by the reduction in the residuals seen in Figure A4, considerably more variance remains after the “enhanced” phase-averaging. The scalar tendencies from the buoy and thermistor records show similar improvements as well. For example, the variance remaining for $\partial/\partial t$ of the near-bottom salinity increases from $r^2=0.32$ to $r^2=0.53$. These variance ratios indicate that the “enhanced” methodology reduces the residual variance by about a factor of two and adjusting for the fortnightly and monthly phase “wobble” in this manner is a substantial improvement over the “plain” phase-averaging of equation (A1a). Note that the same sinusoidal function of M_2-s_2 and M_2-a_2 frequencies was used for all the enhanced phase-averaging used herein, with the coefficients determined by harmonic analysis of the along-channel component of the near-bottom ADCP1 record.

Acknowledgments

The operation of the Long Island Sound Integrated Coastal Observing System (LISICOS) and the analysis presented here were supported by the National Oceanic and Atmospheric Administration through the North East Regional Association of Coastal Ocean Observation Systems (NERACOOS). Data are available from: <http://lisicos.uconn.edu/>.

References

- Bennett, D. C., J. O'Donnell, W. F. Bohlen, and A. Houk (2010), Tides and overtides in long Island Sound, *J. Mar. Res.*, *68*, 1–35.
- Blumberg, A. F., and D. W. Pritchard (1997), Estimates of the transport through the East River, New York, *J. Geophys. Res.*, *102*(C3), 5685–5703.
- Bourgault, D., and D. E. Kelley (2003), Wave-induced boundary mixing in a partially mixed estuary, *J. Mar. Res.*, *61*, 553–576.
- Burchard, H. (2002), *Applied Turbulence Modeling in Marine Waters*, Springer-Verlag, Berlin, Heidelberg.
- Chant, R., W. Geyer, R. Houghton, E. Hunter, and J. Lerczak (2007), Estuarine boundary layer mixing processes: Insights from dye experiments, *J. Phys. Oceanogr.*, *37*, 1859–1877.
- Colosi, J. A., R. C. Beardsley, J. F. Lynch, G. Gawarkiewicz, C. S. Chiu, and A. Scotti (2001), Observations of nonlinear internal waves on the outer New England continental shelf during the summer Shelfbreak Primer study, *J. Geophys. Res.*, *106*(C5), 9587–9601.
- Garrett, C., and W. Munk (1979), Internal waves in the Ocean, *Am. Rev. Fluid Mech.*, *11*, 339–369.
- Gay, P. S., J. O'Donnell, and C. Edwards (2004), Exchange between Long Island Sound and adjacent waters, *J. Geophys. Res.*, *109*, C06017, doi:10.1029/2004JC002319.
- Helda, P., K. Schrottker, and A. Bartholomäb (2013), Generation and evolution of high-frequency internal waves in the Ems estuary, Germany, *J. Sea Res.*, *78*, 25–35.
- Henye, F. S. (1999), Exact Solitary Wave Solutions in Shallow Water, paper presented at Aha Huliko'a Hawaiian Winter Workshop, Univ. of Hawaii SOEST. [Available at <http://www.soest.hawaii.edu/PubServices/1999pdfs/Henye.pdf>]

- Hosegood, P., and H. van Haren (2004), Near-bed solibores over the continental slope in the Faeroe-Shetland Channel, *Deep Sea Res., Part II*, 51, 2943–2971.
- Jackson, C. (2004), *An Atlas of Internal Solitary-like Waves and their Properties*, 2nd ed., Global Ocean Associates, ONR contract N00014-03-C-0176, Alexandria, Va.
- Li, M., J. Trowbridge, and R. Geyer (2007), Asymmetric tidal mixing due to the horizontal density current, *J. Phys. Oceanogr.*, 38, 418–434.
- Lien, R.-C., and M. C. Gregg (2001), Observations of turbulence in a tidal beam across a coastal ridge, *J. Geophys. Res.*, 106(C3), 4575–4591.
- MacKinnon, J. A., and M. C. Gregg (2005), Spring mixing: Turbulence and internal waves during restratification on the New England shelf, *J. Phys. Oceanogr.*, 35, 2425–2442.
- McCardell, G., and J. O'Donnell (2009), A novel method for estimating vertical eddy diffusivities using diurnal signals with application to western Long Island Sound, *J. Mar. Syst.*, 77, 397–408, doi:10.1016/j.jmarsys.2008.10.011.
- McCardell, G., and J. O'Donnell (2014), Estimates of horizontal fluxes of oxygen, heat, and salt in western Long Island Sound, *J. Geophys. Res. Oceans*, 119, 7267–7276, doi:10.1002/2014JC009904.
- McCready, P., and W. R. Geyer (2010), Advances in estuarine physics, *Annu. Rev. Mar. Sci.*, 2, 35–58.
- Mellor, G. L., and T. Yamada (1982), Development of a turbulence closure model for geophysical fluid problems, *Rev. Geophys. Space Phys.*, 20, 851–875.
- Morgan, P. P. (1998), Matlab Seawater Library, v2.01, Commonwealth Scientific and Industrial Research Organisation.
- Moum, J. N., D. M. Farmer, W. D. Smyth, L. Armi, and S. Vagle (2003), Structure and generation of turbulence at interfaces strained by internal solitary waves propagating shoreward over the continental shelf, *J. Phys. Oceanogr.*, 33, 2093–2112.
- Müller, P., and M. Briscoe (2000), Diapycnal mixing and internal waves, *Oceanography*, 13(2), 98–103. [Available at <http://dx.doi.org/10.5670/oceanog.2000.40>.]
- Munk, W. H., and E. R. Anderson (1948), Notes on a theory of the thermocline, *J. Mar. Res.*, VII(3), 276–295.
- Munk, W. H., and C. Wunsch (1998), Abyssal recipes II: Energetic of tides and mixing, *Deep Sea Res., Part I*, 45, 1977–2010.
- O'Donnell, J., H. G. Dam, W. F. Bohlen, W. Fitzgerald, P. Gay, A. E. Houk, D. C. Cohen, M. M. Howard-Strobel (2008), Intermittent ventilation in the Hypoxic Zone of western long Island Sound during the summer of 2004, *J. Geophys. Res.*, 113, C09025, doi:10.1029/2007JC004716.
- O'Donnell, J., R. E. Wilson, K. Lwiza, M. Whitney, W. F. Bohlen, D. Codiga, D. B. Fribance, T. Fake, M. Bowman, and J. Varekamp (2014), The physical oceanography of long Island sound, in *Long Island Sound: Prospects for the Urban Sea*, edited by J. S. Latimer et al., 79–158, Springer, N. Y.
- Rippeth, T. P., N. R. Fisher, and J. H. Simpson (2001), The cycle of turbulent dissipation in the presence of tidal straining, *J. Phys. Oceanogr.*, 31, 2458–2471.
- Sharples, J., J. H. Simpson, and J. M. Brubaker (1994), Observations and modeling of periodic stratification in the upper York River estuary, *Estuarine Coastal Shelf Sci.*, 38, 301–312.
- Simpson, J. H., J. Brown, J. Matthews, and G. Allen (1990), Tidal straining, density currents, and stirring in the control of estuarine stratification, *Estuaries*, 13, 125–132.
- Thorpe, S. A. (2005) *The Turbulent Ocean*, Cambridge Univ. Press, Cambridge, N. Y.
- Umlauf, L., and H. Burchard (2005), Second-order turbulence closure models for geophysical boundary layers. A review of recent work, *Cont. Shelf Res.*, 25, 795–827.
- Whitney, M., D. L. Codiga, D. S. Ullman, P. M. McManus, and R. Jorle (2012), Tidal cycles in stratification and shear and their relationship to gradient Richardson number and eddy viscosity variations in estuaries, *J. Phys. Oceanogr.*, 42, 1124–1133, doi:10.1175/JPO-D-11-0172.1.